Original Article

A Validated Mathematical Model of FGFR3-Mediated Tumor Growth Reveals Pathways to Harness the Benefits of Combination Targeted Therapy and Immunotherapy in Bladder Cancer

Kamaldeen Okuneye[1] Daniel Bergman[2] Jeffrey C. Bloodworth[3] Alexander T. Pearson[4,*] Randy F. Sweis[3,*] Trachette L. Jackson[2,*]

[1] Applied BioMath, LLC, Concord, Massachusetts, USA; kokuneye@appliedbiomath.com

[2] Department of Mathematics, University of Michigan, Ann Arbor, MI 48109, USA; bergmand@umich.edu

[3] Department of Medicine, Section of Hematology/Oncology, The University of Chicago, 5841 S Maryland Ave, MC 2115, Chicago, IL 60605 USA; rsweis@medicine.bsd.uchicago.edu

[4] Department of Medicine, Section of Hematology/Oncology, The University of Chicago, Chicago, IL 60637, USA; apearson5@medicine.bsd.uchicago.edu

[*] Correspondence: tjacks@umich.edu, rsweis@medicine.bsd.uchicago.edu, and apearson5@medicine.bsd.uchicago.edu

Running Title:

Modeling FGFR3-Targeted and anti-PD-L1 Therapy

Keywords:

mathematical model, FGFR3-targeted therapy, immune checkpoint inhibitors, bladder cancer

Acknowledgments:

This work was supported by NIH/NCI U01CA243075 (ATP, RFS, TLJ).

Submitted: December 30th, 2020

Abstract

Bladder cancer is a common malignancy with over 80,000 estimated new cases and nearly 18,000 deaths per year in the United States alone. Therapeutic options for metastatic bladder cancer had not evolved much for nearly four decades, until recently, when five immune checkpoint inhibitors were approved by the FDA. Despite the activity of these drugs in some patients, the objective response rate for each is less than 25%. At the same time, fibroblast growth factor receptors (FGFRs) have been attractive drug targets for a variety of cancers, and in 2019 the FDA approved the first therapy targeted against FGFR3 for bladder cancer. Given the excitement around these new receptor tyrosine kinase and immune checkpoint targeted strategies, and the challenges they each may face on their own, emerging data suggest that combining these treatment options could lead to improved therapeutic outcomes. In this paper, we develop a mathematical model for FGFR3-mediated tumor growth and use it to investigate the impact of the combined administration of a small molecule inhibitor of FGFR3 and a monoclonal antibody against the PD-1/PD-L1 immune checkpoint. The model is carefully calibrated and validated with experimental data before survival benefits and dosing schedules are explored. Predictions of the model suggest that FGFR3 mutation reduces the effectiveness of anti-PD-L1 therapy, that there are regions of parameter space where each monotherapy can outperform the other, and that pretreatment with anti-PD-L1 therapy always results in greater tumor reduction even when anti-FGFR3 therapy is the more effective monotherapy.

1 Introduction

Bladder cancer is one of the 10 most common cancers in the United States and in advanced stages 5-year survival rates are low (below 35%) [1]. For more than 30 years, therapeutic strategies have focused on the use of systemic chemotherapy before, during, or after loco-regional therapy [2]. Unfortunately, outcomes with chemotherapy are poor in advanced cases [3]. For this reason, researchers have turned their attention to targeted therapies.

Members of the fibroblast growth factor receptor (FGFR) family have become a successful therapeutic focal point for bladder cancer [4]. Genomic analysis of bladder cancer has identified

frequent alterations of FGFRs, including over-expression and mutations of FGFR3 that activate the receptor via ligand-independent dimerization [4]. Under normal conditions, heparin bound fibroblast growth factor (FGF) mediates FGFR3 dimerization, leading to kinase activation and stimulation of the extracellular-signal-regulated kinase (ERK) and protein kinase B (AKT) signaling pathways, followed by increased cell proliferation and cell survival [4]. FGFR3 mutations that lead to constitutive activation of downstream signaling pathways in the absence of FGF are commonly found in bladder cancers. Urothelial bladder carcinoma has the most established association with altered FGFR3 signaling, with up to 80% of low-grade tumors harboring FGFR3 mutations [5]. Clinical trials using small molecule inhibitors (SMIs) of FGFR3 show promising clinical responses for patients with FGFR3 mutations and in 2019, the FDA approved the first therapy targeted against FGFR3 [4].

At the same time, immunotherapy has now emerged as an exciting domain for exploration for many cancers including bladder cancer. The recent success of programmed cell death protein 1 (PD-1) and programmed death-ligand 1 (PD-L1) blockade in cancer therapy illustrates the important role of the PD-1/PD-L1 checkpoint in the regulation of anti-tumor immune responses [6]. In particular, monoclonal antibodies (mAbs) targeting the PD-1/PD-L1 pathway have resulted in favorable outcomes in advanced bladder cancer and 6 immune checkpoint inhibitors (ICIs) targeting this pathway were approved in 2015-2018 [7]. Despite therapeutic potential of ICIs, only a minority (approximately 20%) of bladder cancer patients respond favorably to these therapies and median survival with second line immunotherapy remains shorter than 1 year [8]. Figure 1 is a schematic diagram showing the impact of FGFR3 mutations and PD-1-PD-L1 checkpoints on tumor growth and tumor cell - T cell interactions.

Given the potential and challenges ICIs on their own, it is possible that the co-acting combination of potent immune checkpoint inhibitors and specific FGFR3 inhibitors can offer much-needed improvements in targeted therapeutics for bladder cancer. The the rationale for combining FGFR3-targeted therapy with immunotherapy is confirmed in preclinical and correlative literature and animal models suggest potential synergies between these two mechanisms [8]. When attempting to combine two very different therapeutic approaches that target distinct pathways, treatment out-

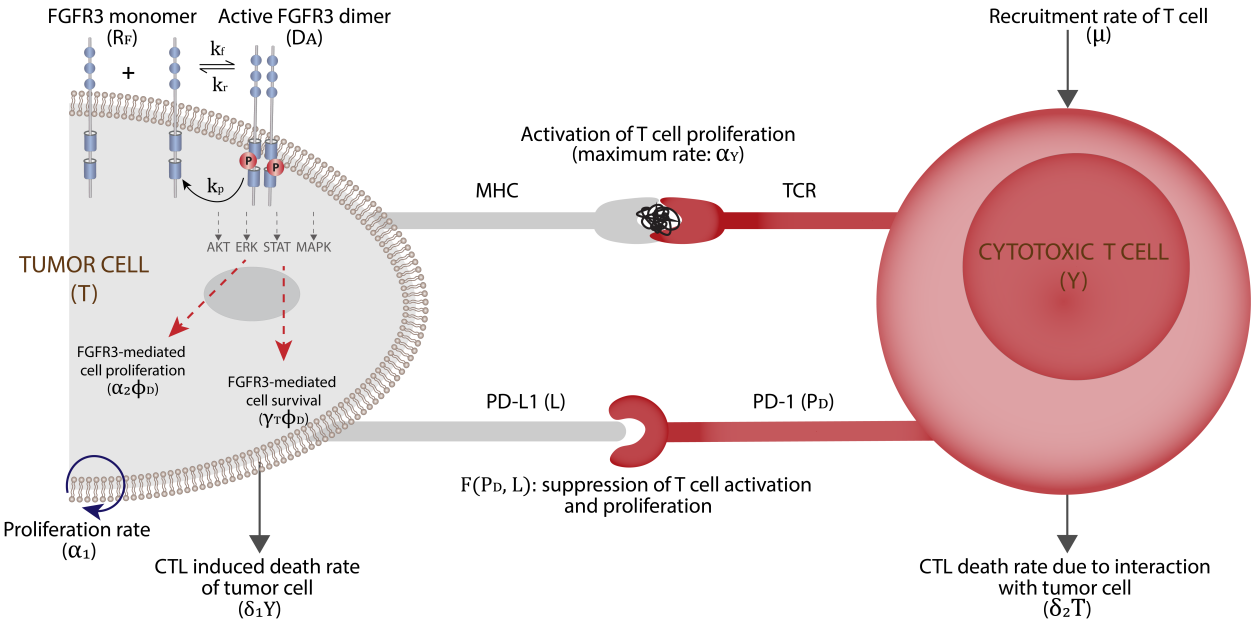

FIGURE 1. Microenvironment of tumor cell showing the dynamics of FGFR3 mutation on tumor cells (phosphorylation of the kinase region leads activation of AKT, ERK, STAT, and MAPK proteins which result into target DNA transcription leading to cell proliferation and cell survival), the activation of T cell by tumor cells, and suppression of T cell activation and proliferation by PD-L1 binding with PD-1.

comes can depend on the order and timing in which therapies are administered. Experimental studies of the most appropriate strategy for FGFR3 inhibition in the context of ICI therapy (either through sequencing or combination) are generally in early clinical stages. Data driven mathematical modeling is an ideal tool for analyzing novel drug combinations for clinical cancer treatment and here we design a model to investigate FGFR3 mediated tumor growth and response to combination targeted and ICI therapy. The sections below describe the details of model development, sensitivity and identifiability analysis, parameter estimation, and therapeutic predictions.

2 Model Formulation

Our mathematical model is based on the current biological understanding of bladder cancer growth when the FGFR3 mutation is present. We first develop a pretreatment model that describes the impact of ligand-independent activation of FGFR3 on tumor growth and CTL mediated death. Next, we extend the pretreatment model to include anti-PD-L1 therapy alone and in combination

with FGFR3-targeted therapy. These models are used to predict the impact of therapy on survival outcomes and to suggest the best dose scheduling regimes for therapeutic efficacy.

2.1 Model Formulation with FGFR3 and Immune Checkpoints

The pretreatment model, described in detail below, captures the local evolution of free FGFR3 (R) and active FGFR3 dimer complexes (D) on tumor cells (T) as well as PD-1 (P_D) and PD-L1 (L) mediated immune cell (Y) kill. The model variables and their units are described in Table 1.

TABLE 1. Description of Variables

Variable	Description	Units
R	Free FGFR3 monomer receptors	nmol
D	Active FGFR3 dimer complexes	nmol
T	Tumor cells	cells
Y	Cytotoxic T cells (CTL)	cells
P_D	PD-1	nM
L	PD-L1	nM

The equations in (1) below describe the ligand-independent dimerization of FGFR3. Parameters that mediate these FGFR3 dynamics include the receptor association rate (k_f) and dissociation rate (k_r). It is also known that activated receptors undergo stimulated endocytosis but can continue to signal along the endocytic pathway [9] so we also include terms for receptor internalization and recycling rate (k_p). For a full list of parameters see Table 2.

$$\begin{aligned} \frac{dR}{dt} &= -2k_f R^2 + 2k_r D + 2k_p D + R_T \mathscr{P}(T, \phi_D) - \frac{R}{R+2D} R_T \mathscr{D}(T, Y, \phi_D) \\ \frac{dD}{dt} &= k_f R^2 - k_r D - k_p D - \frac{D}{R+2D} R_T \mathscr{D}(T, Y, \phi_D) \end{aligned} \tag{1}$$

These ODEs must account for changes in receptor number due to cellular proliferation and apoptosis. The last two terms in the equation for free receptors (R) describes the generation of new receptors as cells divide and the loss of receptors as cells die, respectively, where R_T is the total number of FGFR3 molecules on tumor cells and $\frac{R}{R+2D}$ is the fraction of free FGFR3 that is removed from the loss of tumor cells (T) by cytotoxic T cells (Y). The FGFR-dependent proliferation growth and death rates of tumor cells (i.e., $\mathscr{P}(T, \phi_D)$ and $\mathscr{D}(T, Y, \phi_D)$ are defined in the temporal dynamics of

the tumor cells described below, where ϕ_D is the fractional occupancy of active FGFR3 dimer per cell defined by:

$$\phi_D = \frac{1}{R_T}\frac{D}{T}. \tag{2}$$

Equation (3) below models the temporal dynamics of the tumor cells

$$\frac{dT}{dt} = (\alpha_1 + \alpha_2\phi_D)T - \frac{\delta_1 Y}{1+\gamma_T\phi_D}T \equiv \mathscr{P}(T,\phi_D) - \mathscr{D}(T,Y,\phi_D) \tag{3}$$

The first term in Equation (3) describes tumor cells with high antigenicity proliferating exponentially with a natural growth rate α_1, and an FGFR-mediated tumor growth rate α_2. The second term in Equation (3) describes the killing of tumor cells by cytotoxic T cells (Y) modified by the impact of FGFR3 on tumor survival, where δ_1 is the death rate of a tumor cell by cytotoxic T cells, and γ_T is the sensitivity of fractional occupancy of FGFR. This formulation assumes that the total number (converted to nmol using molecular weight) of receptors per tumor cell R_T remains constant. This means that the total amount of FGFR3 in the system should be conserved. We can ensure that the model equations do conserve FGFR3 by considering the sum of the equations of the model (1):

$$\frac{dR}{dt} + 2\frac{dD}{dt} = R_T\left[\mathscr{P}(T,\phi_D) - \mathscr{D}(T,Y,\phi_D)\right] = R_T\frac{dT}{dt},$$

Therefore, upon integration, we have

$$R + 2D = R_T T.$$

The equation for the change in cytotoxic T cells (Y) is given by:

$$\frac{dY}{dt} = \left(\mu + \alpha_Y\frac{T}{\kappa+T}Y\right)F(P_D,L) - \delta_2 TY - \delta_Y Y \tag{4}$$

The first term in Equation (4) represents a constant recruitment/activation of T cells at a rate, μ. The second term describes proliferation that occurs as the result of antigenic stimulation by the tumor cells. The maximum proliferation rate is α_Y and κ represents the population of T at which the

immune cells lyse tumor cells at half of their maximum killing rate [10]. The factor $F(P_D, L)$, which is described in greater detail below, represents the suppression of T cell activation and proliferation via the PD-1/PD-L1 checkpoint. The variables P_D and L denote the molar concentrations of PD-1 and PD-L1, respectively, expressed by cells within the model. The molar concentrations are obtained by first calculating the PD-1 expression on all T cells and the PD-L1 expression on all T cells and tumor cells as outlined in the Appendix found in [10]. Our formulation of $F(P_D, L)$ in Equation (7) below ensures that as P_D and L increases so does the number of PD-1/PD-L1 complexes within the tumor region. This increase corresponds to a smaller $F(P_D, L)$ value, modeling the inhibition of T cell activity. Finally, the last two terms describe how CTLs can die. Specifically, interaction with tumor cells can result in death at a rate δ_2 as was done in [11], but which sets our model apart from [10, 12, 13]. CTLs can also die naturally at a rate δ_Y.

We assume that all T cells express PD-1 and that the temporal dynamics of this cell-bound protein is proportional to the rate of change of the T cells on which they reside as described by Equation 5. This is the same approach used in [10, 12, 13].

$$\frac{dP_D}{dt} = \rho_P \frac{dY}{dt} \qquad \Rightarrow \qquad P_D = \rho_P Y \tag{5}$$

where, ρ_P is the cell rate of expression of PD-1 on T cells. Again, following [10, 12, 13], the molar concentration of PD-L1 (L) within the tumor micro-environment is given by

$$L = \rho_L (Y + \epsilon T) \tag{6}$$

where ρ_L is the is the molar concentration of PD-1 per T cell and the parameter $\epsilon > 1$ reflects the fact that the expression of PD-L1 is upregulated on tumor cells (and depends on the specific type of tumor). Finally, we choose the following functional form for T cell suppression via PD-1 signaling, $F(P_D, L)$, just as in [10, 12, 13] by

$$F(P_D, L) = \frac{1}{1 + P_D L / K_{YQ}}. \tag{7}$$

The parameter values and their sources for the full pretreatment model are provided in Table 2.

TABLE 2. Pretreatment Parameter Values

Variable	**Description**	**Range of value** (Baseline)	**Units**	**Source**
FGFR3-related				
k_f	FGFR3 association rate	$1 - 5 \times 10^{11}\,(4.16 \times 10^{11})$	$\text{nmol}^{-1}\,\text{d}^{-1}$	[14]
k_r	FGFR3 dissociation rate	$10 - 2000\,(864)$	d^{-1}	[14]
k_p	FGFR3 recycling rate	$10 - 150\,(112.32)$	d^{-1}	[14]
R_T	Total FGFR3 receptors	$1.49 - 1.74 \times 10^{-11}\,(1.66 \times 10^{-11})$	$\text{nmol}\,\text{cell}^{-1}$	[15]
Tumor-related				
α_1	Proliferation rate	$0.12 - 0.51\,(0.337)$	d^{-1}	Best fit
α_2	FGFR3-mediated proliferation rate	$0.001 - 0.1\,(0.00774)$	d^{-1}	Best fit
δ_1	CLT-mediated death rate	$1 - 2.5 \times 10^{-7}\,(1.1 \times 10^{-7})$	$\text{cell}^{-1}\,\text{d}^{-1}$	[11]
γ_T	FGFR3-enhanced survival sensitivity	$0.1 - 0.5\,(0.3018)$		Best fit
T cell-related				
μ	Activation/recruitment rate	$1 - 2 \times 10^{4}\,(1.3 \times 10^{4})$	$\text{cell}\,\text{d}^{-1}$	[11]
α_Y	Max proliferation rate	$0.1 - 0.5\ (0.3044)$	d^{-1}	[11, 12, 16]
κ	Proliferation half-saturation constant	$10^6 - 3 \times 10^7 (2.019 \times 10^7)$	cell	[11]
δ_2	Tumor-mediated death rate	$2 - 4 \times 10^{-10}\,(3.422 \times 10^{-10})$	$\text{cell}^{-1}\,\text{d}^{-1}$	[11]
δ_Y	Natural death rate	$0 - 0.05\ (0.0412)$	d^{-1}	[10]
ρ_P	PD-1 per cell	$10^{-9} - 10^{-7}\,(1.258 \times 10^{-8})$	nM	[10]
ρ_L	PD-L1 per cell	$10^{-9} - 2 \times 10^{-7}\,(2.51 \times 10^{-8})$	nM	[10]
ϵ	Tumor - immune PD-L1 ratio	$1 - 100\ (50)$		[10, 12, 16]
K_{YQ}	Immune checkpoint inhibition constant	$10^{-4} - 10^{-2}\,(1.296 \times 10^{-3})$	nM^2	[10]

2.2 Model Formulation with FGFR3, Immune Checkpoints, and Combination Therapy

In this section, we extend our pretreatment model equations to incorporate the therapeutic administration of an immune checkpoint inhibitor (ICI) in the form of a monoclonal antibody against

PD-L1 and a small molecule inhibitor (SMI) targeting the FGFR3 pathway. We refer to the former as anti-PD-L1 therapy and the latter as anti-FGFR3 therapy and our goal is to study the response of tumor cells to these therapies alone and in combination. See Figure 2 for a schematic description of a tumor cell undergoing anti-FGFR3 and anti-PD-L1 combination therapy.

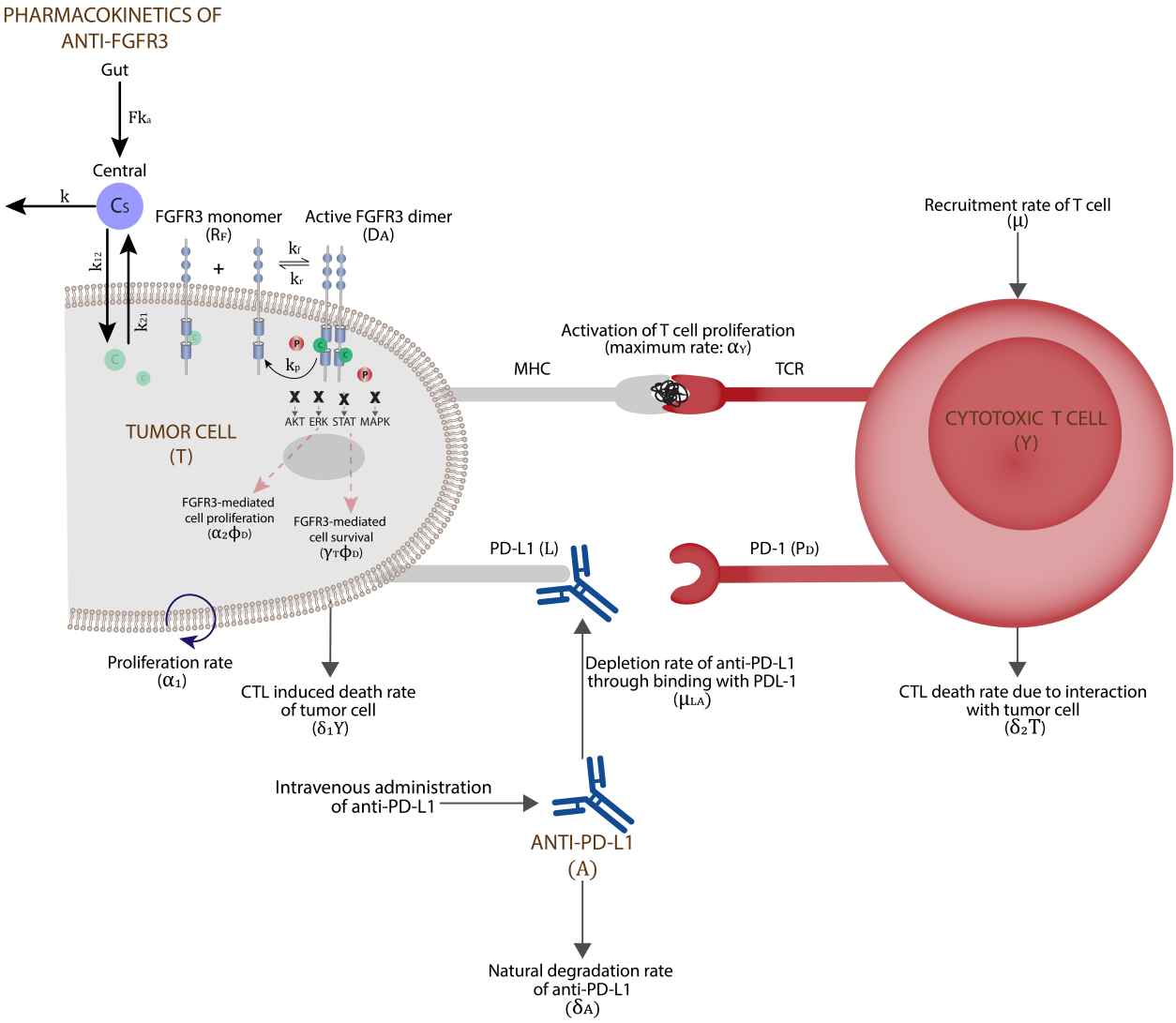

FIGURE 2. Microenvironment of tumor cell with combination therapy of anti-FGFR3 drug plus anti-PD-L1 antibody. We assume that anti-FGFR3 drug binds with both FGFR3 monomers and dimers. Anti-PD-L1 antibody targets PD-L1, thus inhibiting its binding with PD-1 and enabling T cell activation and proliferation.

An anti-PD-L1 antibody (A) binds to PD-L1 and inhibits the formation of the PD-1-PD-L1

complex. Following [10, 12, 13], the equation for the change in anti-PD-L1 antibody is given by:

$$\frac{dA}{dt} = -\mu_{LA} L A - \delta_A A, \tag{8}$$

with an initial condition, $A(0)$, that represents the amount of anti-PD-L1 antibody administered via intraperitoneal injection at different time points, μ_{LA} is the depletion rate of anti-PD-L1 antibody through binding with PDL-1 (L) and δ_A is the natural degradation rate of anti-PD-L1 antibody. Upon administration of an anti-PD-L1 antibody, the equation for the change in cytotoxic T cells (given in Equation (4)) is modified and given by:

$$\frac{dY}{dt} = \left(\mu + \alpha_Y \frac{T}{\kappa + T} Y\right) F(P_D, L, A) - \delta_2 T Y - \delta_Y Y. \tag{9}$$

The functional form $F(P, L, A)$ given by:

$$F(P_D, L) = \frac{1}{1 + \dfrac{P_D L}{K_{YQ}} \left(1 - \dfrac{A}{A + K_D}\right)}. \tag{10}$$

where K_D is the dissociation constant of the PD-L1/anti-PD-L1 complex. The factor $F(P_D, L, A)$ represents the impact of an anti-PD-L1 by reducing the number of PD-1/PD-L1 complexes within the tumor region. In the absence of an anti-PD-L1 antibody (i.e., $A = 0$), the factor $F(P_D, L, A)$ becomes $F(P_D, L)$ given by Equation (7). See Appendix A for the full derivation of $F(P_D, L, A)$.

By binding to the kinase activity region of the receptors, an anti-FGFR3 drug (rogaratinib) inhibits the phosphorylation of the FGFR3 kinase domain and the downstream signaling of AKT, MAPK, ERK, and STAT [17, 18, 19]. To incorporate the therapeutic administration of rogaratinib, we designed a pharmacokinetic model with oral administration of rogaratinib. We assume that the tumor resides in a pharmacokinetic compartment of its own, and rogaratinib is transferred into the tumor from the systemic circulation at the same rate as the peripheral tissue. The pharmacokinetics of rogaratinib and the system of equations (and all the underlying assumptions) governing the dynamics of FGFR3 in the tumor cell in the presence of rogaratinib are given in Appendices B and C, respectively.

Overall, the temporal dynamics of the tumor cells in the presence of combination therapy of anti-FGFR3 and anti-PD-L1 is given by:

$$\frac{dT}{dt} = (\alpha_1 + \alpha_2\phi_D^C)T - \frac{\delta_1 Y}{1+\gamma_T\phi_D^C}T \equiv \mathscr{P}(T,\phi_D^C) - \mathscr{D}(T,Y,\phi_D^C) \tag{11}$$

where ϕ_D^C is the fractional occupancy of active FGFR3 dimer per cell in the presence of anti-FGFR3 drug (described in Appendix A) and the temporal dynamics of cytotoxic T cells (Y) are given by Equation (9).

3 Pretreatment Results

3.1 Parameter Sensitivity

We use uncertainty and sensitivity analysis to determine the parameters that have the greatest effect on tumor growth in the FGFR3 mutation model without treatments (Equations (1), (3), and (4)). Global sensitivity analysis quantifies the impact of the variations or sensitivity of each parameter of the model on the model outcomes [20, 21, 22]. In particular, following [21, 22], Latin hypercube sampling (LHS), and the partial rank correlation coefficient (PRCC) will be used for this analysis. The sensitivity analysis of the model is carried out using the tumor volume (in mm^3) at the final time point, which is defined as $\frac{T(t_f)}{10^6}$ where $t_f = 25\,\text{d}$. The range and baseline values of the parameters, tabulated in Table 2, will be used. The result depicted in Figure 3 shows that the parameters that significantly affect the tumor growth dynamics are the natural growth rate of tumor cells (α_1), the CTL mediated death rate of tumor cells (δ_1), and FGFR3-mediated tumor proliferation (α_2), and the sensitivity of tumor survival to FGFR3 (γ_T). Overall, these results indicate that therapies (monotherapies or combination therapies) that reduce the natural growth rate of tumor cells, increase the death rate of tumor cells by cytotoxic T-cells (e.g. the use of antibodies to target the immune checkpoint PD-1/PD-L1 pathway to active cytotoxic T-cells), and/or decreasing fractional occupancy of FGFR3 dimer complexes on tumor cells (e.g., the use of anti-FGFR3 drugs to target the FGFR3 pathway) will be effective in controlling and treating bladder cancer with FGFR3 mutation.

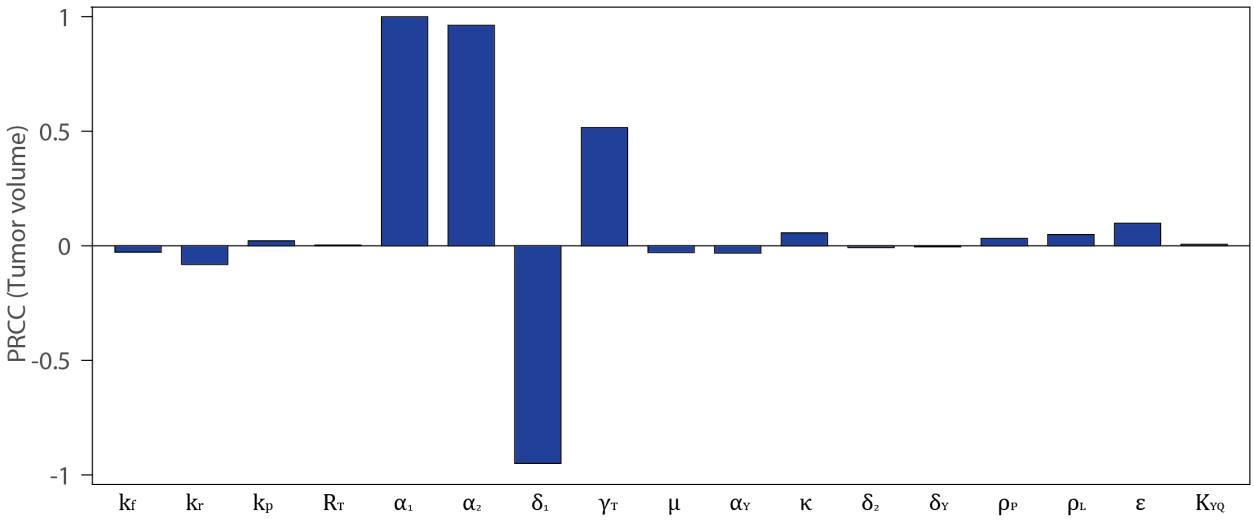

FIGURE 3. Sensitivity analysis of models (1), (3), and (4) showing PRCC values for the model parameters using the tumor volume as a response function. The baseline and range of parameter values used are given in Table 2.

3.2 Pretreatment Identifiability

To determine which model parameters, if any, can be uniquely estimated from a given data set (and to what degree of certainty), we employ identifiability analysis [23]. This toolkit allows us to determine the subset(s) of identifiable parameters and explore their interplay without even using experimental data for parameter estimation and model calibration [24]. We examine both structural and practical identifiability of the model parameters.

3.2.1 Structural Identifiability

First, we perform a structural identifiabilty analysis to determine whether or not it is possible to obtain a unique solution for the parameters while assuming perfect data (noise-free and continuous in time and space) [25, 26, 27, 28]. Specifically, we consider the subset of the sensitive parameters identified in Section 3.1 and determine if they can be uniquely estimated from measurements of values of all the model variables (active dimer complexes on tumor cells, tumor volume, and the number of cytotoxic T cells). The structural identifiability of the model is analyzed using the

MATLAB package GenSSI (see [25, 28] for complete details).

We obtained an identifiability tableau in Figure 4A that shows 8 non-zero rows–indicated by black regions and corresponding to non-zero generating series coefficients–that depend on the sensitive parameters. If any parameters from the identifiability tableau can be computed as functions of the power series coefficients and eliminated, then a reduced tableau is obtained [25], as shown in Figure 4B. Using the GenSSI algorithm, we obtained unique solutions for all the sensitive parameters $(\alpha_1, \delta_1, \alpha_2, \gamma_T)$, that is, they are globally identifiable. Thus, the model is globally structurally identifiable, which indicates that error-free time series data of all the model variables would be sufficient to identify a unique subset of the four parameters.

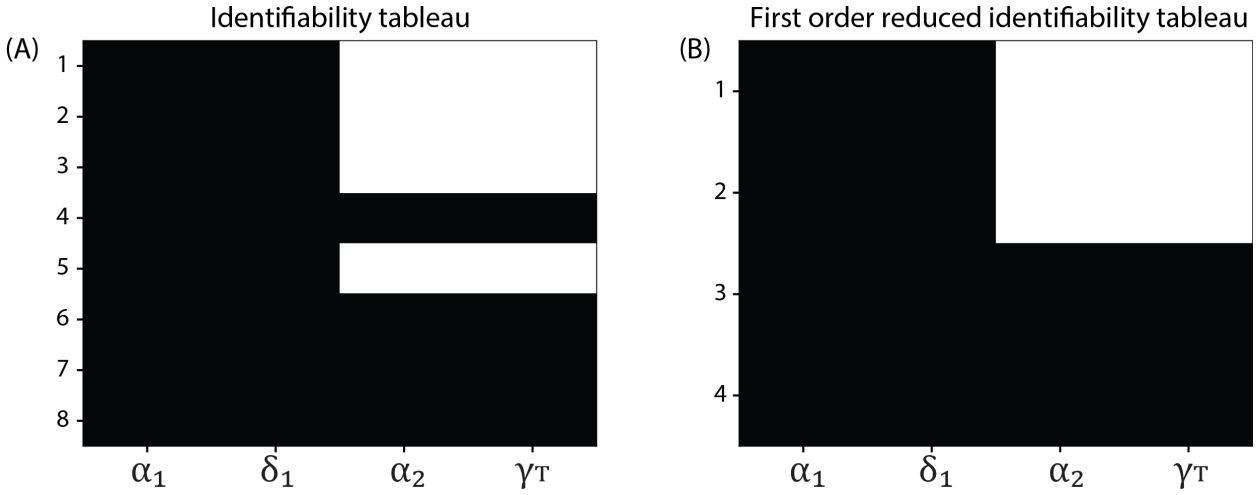

FIGURE 4. Model identifiability results with the subset of four most sensitive parameters the model. (A) Identifiability tableau. (B) Results and reduced tableau. All four parameters shown are globally identifiable.

3.2.2 Practical Identifiability

In practice, complete time-series and noiseless experimental data for structural identifiability are not available. Therefore, in this section, we carry out a practical identifiability analysis to determine whether the most-sensitive parameters are identifiable from noisy experimental data of tumor volume. To do this, we seek to determine whether a distribution with a clear mode can be determined for each of the sensitive parameters given such data. We used the Markov chain Monte Carlo

(MCMC) method with Metropolis-Hastings sampling [25]. Given simulated data for the system output, prior distributions of the parameter values, and a likelihood function, the MCMC samples the posterior distributions of the parameter, and the Metropolis-Hastings updating scheme accepts the new sample with probability given by the ratio of the new likelihood to the old likelihood [25].

Specifically, we use uniform distributions as prior distributions on the parameters within the ranges given in Table 2. To create the likelihood functions, we use the experimental data for tumor volume without FGFR3 mutation – to determine the practical identifiability of α_1 and δ_1 – and the experimental data for tumor volume with FGFR3 mutation – to determine the practical identifiability of α_2 and γ_T. The tumor volume for each day is assumed to be log-normally distributed about the mean tumor volume at each time point and truncated to be within one standard deviation of this mean. The joint probability distribution of these is then used to create the likelihood functions for the two applications of the MCMC method. We first used MCMC to estimate the posterior distributions for α_1 and δ_1 and then separately used it for α_2 and γ_T. In both cases, we used a chain length of 10,000 to sample from the posterior distributions.

The result depicted in Figure 5A in the form of one-dimensional histograms and two-dimensional heat maps shows that α_1 has a normal distribution and δ_1 has a broad distribution within its range in Table 2, thus indicating that α_1 is practically identifiable and δ_1 is not practically identifiable. Then, by sampling from this posterior distribution and forward simulating, we generate model predictions of tumor volume distributions without FGFR3 mutation at the sample time points that are tightly controlled and match the corresponding distributions from the data (Figure 5B). Similarly, using experimental data for mean tumor volume with FGFR3 mutation, our simulation showed that α_2 and γ_T have a normal and a broad distribution, respectively (Figure 5C), within its range in Table 2. Hence, α_2 is practically identifiable, and γ_T is not practically identifiable given the available experimental data. We again sample from the posterior distribution and forward simulate to generate tumor volume distributions with FGFR3 mutation, and again we see that these distributions are tightly controlled and match the corresponding data distribution (Figure 5D).

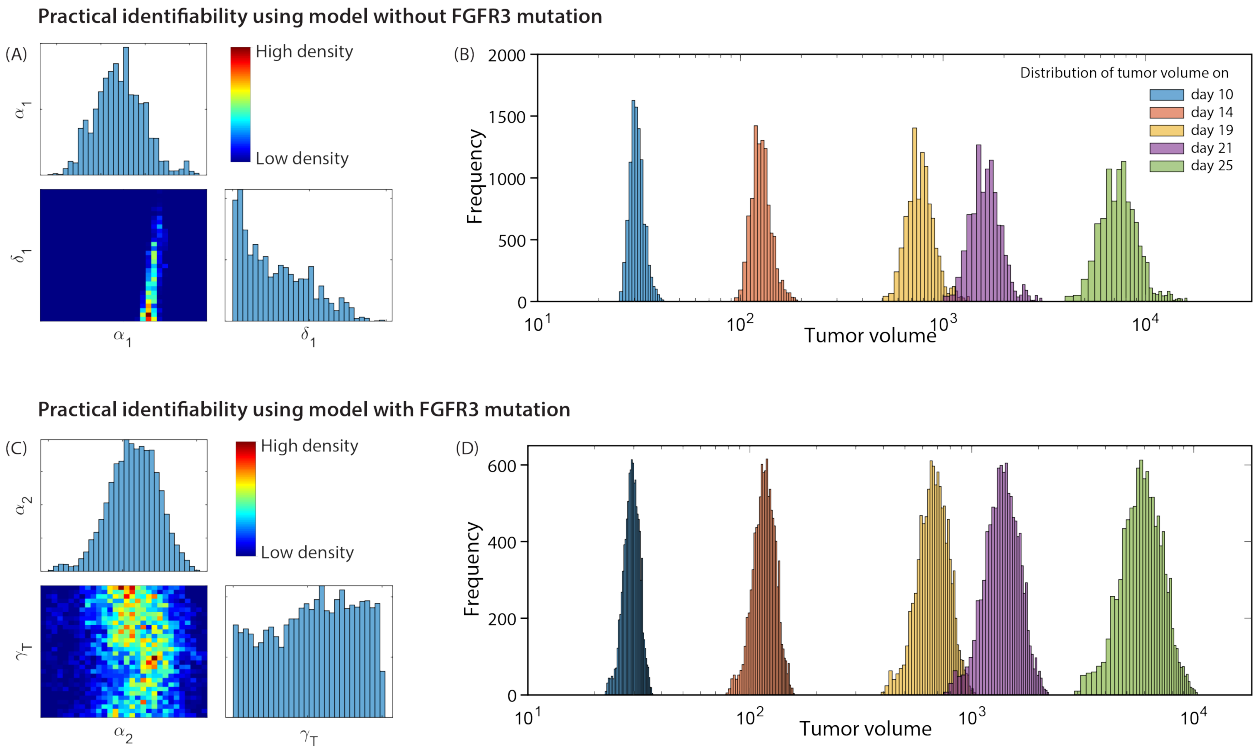

FIGURE 5. (A) Matrix of two-dimensional heat maps with one-dimensional histograms on the diagonal showing the parameter distributions of α_1 and δ_1 using experimental data of tumor volume without FGFR3 mutation. (B) The distributions of tumor volume for the MCMC chain, for five time points using experimental data of tumor volume without FGFR3 mutation. (C) Matrix of two-dimensional heat maps with one-dimensional histograms on the diagonal showing the parameter distributions of α_2 and γ_T using experimental data of tumor volume with FGFR3 mutation (D) The distributions of tumor volume for the MCMC chain, for five time points using experimental data of tumor volume with FGFR3 mutation.

3.3 Pretreatment Experimental Studies

For mouse experiments, 6-8 week old female C57BL/6 mice were obtained from Jackson laboratory. Mice were housed in a specific pathogen-free animal facility at the University of Chicago. The MB49 cell line is a carcinogen-induced urothelial carcinoma cell line derived from a male C57BL/6 mouse, which was generously provided by Timothy L. Ratliff, Purdue University. The MB49-FGFR3G370C cell line was were generated by retroviral transduction using the pMXs-IRES-GFP vector and sorted 4 times for GFP expression. For tumor growth experiments, mice were injected subcutaneously with 1×10^6 MB49-FGFR3G370C tumor cells or GFP vector control MB49 tumor cells. Tumor volume was measured two times per week until endpoint. All experimental animal procedures were approved

by the University of Chicago Animal Care and Use Committee (IACUC).

3.4 Pretreatment Parameter Estimation

Having determined the identifiabilty properties of the most significant parameters both structurally and practically, we turn to estimating these parameters from experimental data. Specifically, we fit the mathematical model to two growth curves of MB49 bladder cancer cell lines, with and without mutant FGFR3 as described above. We use experimental data of tumor volume vs time (5 time points) for 5 mice without mutant FGFR3 to estimate the FGFR3-independent tumor growth rate (α_1). We use the MATLAB lsqcurvefit function with ode15s solver, and an initial condition, given by $T(0) = 10^6$ cells and $Y(0) = 3.2 \times 10^5$ cells [11], to carry out the data-fitting process. By calibrating Equations (3) and (4) with $\alpha_2 = \gamma_T = 0$ with the experimental data (Figure 6A - green curve), we obtained the best fit value for $\alpha_1 = 0.337\,\mathrm{d}^{-1}$, which corresponds to a bladder tumor doubling time of 2.1 days in mice. The box-plot of the residual vector shown in Figure 6B indicates that the model can accurately predict temporal changes tumor volume in mice without the FGFR3 mutation.

With FGFR3-independent parameters estimated, we next calibrate the model with FGFR3 mutation (Equations (1), (3), and (4)). Specifically, we use experimental data of tumor volume vs. time when the FGFR3 mutation is present in mice (Figure 6A - red curve) to estimate two parameters associated with ligand-independent activation of FGFR3 (i.e., the FGFR3-mediated tumor proliferation rate ($\alpha_2 = 0.007\,74\,\mathrm{d}^{-1}$) and the FGFR3-mediated survival sensitivity parameter ($\gamma_T = 0.3018$). As before, we generated box-plots of residuals (Figure 6C), indicating that the model can accurately predict tumor volume when the FGFR3 mutation is active. It is important to note that growth of the experimental tumor cell line is not dependent on the FGFR3 activating mutation, which was exogenously introduced. Thus, we do not expect the FGFR3 activating mutation to have a significant impact on tumor growth as observed in both the data and model simulation.

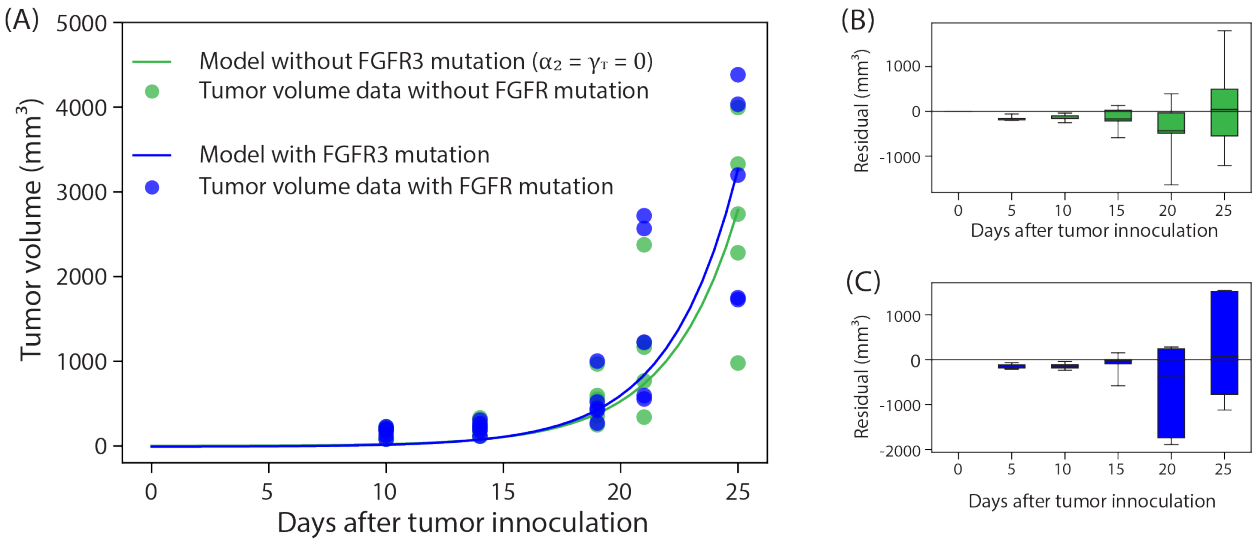

FIGURE 6. (A) Green curve: Calibration of models (3) and (4) with $\alpha_2 = \gamma_T = 0$ to the experimental data of tumor without FGFR3 mutation in mice ($n = 5$) to estimate the FGFR3-independent growth rate ($\alpha_1 = 0.337\,\mathrm{d}^{-1}$). Blue curve: Calibration of models (1), (3), and (4) to the growth curve of tumor with FGFR3 mutation in mice ($n = 5$) to estimate FGFR3-dependent parameters ($\alpha_2 = 0.007\,74\,\mathrm{d}^{-1}$ and $\gamma_T = 0.3018$). (B, C) Residual plots showing that the models predict tumor volume without FGFR3 mutation and with FGFR3 mutation, respectively.

3.5 Relative Impact of FGFR3-dependent Pathways on Tumor Growth

With all parameters associated with tumor growth now estimated, an important question arises about which FGFR3-mediated effect, increased proliferation or increased survival, results in a greater measurable increase in tumor volume. We addressed this by estimating, from simulations, the difference between the tumor volume on day 25 when the FGFR3 survival benefit is switched off (i.e.$\alpha_2 \in [0.001, 0.03]$ and $\gamma_T = 0$) and when the FGFR3 proliferative benefit is turned off (i.e. $\alpha_2 = 0$ and $\gamma_T \in [0.1, 0.5]$). In this way, we compare their relative contributions to tumor growth and in Figure 7 we see that parameter space is divided in two by which mechanism leads to more tumor growth. It is interesting to note that the region in parameter space that corresponds to the proliferation effect resulting in larger tumors is much more expansive. This region also contains the point corresponding to our estimated parameters as shown by the red dot in Figure 7, though the difference in the effect on tumor volume there is slight.

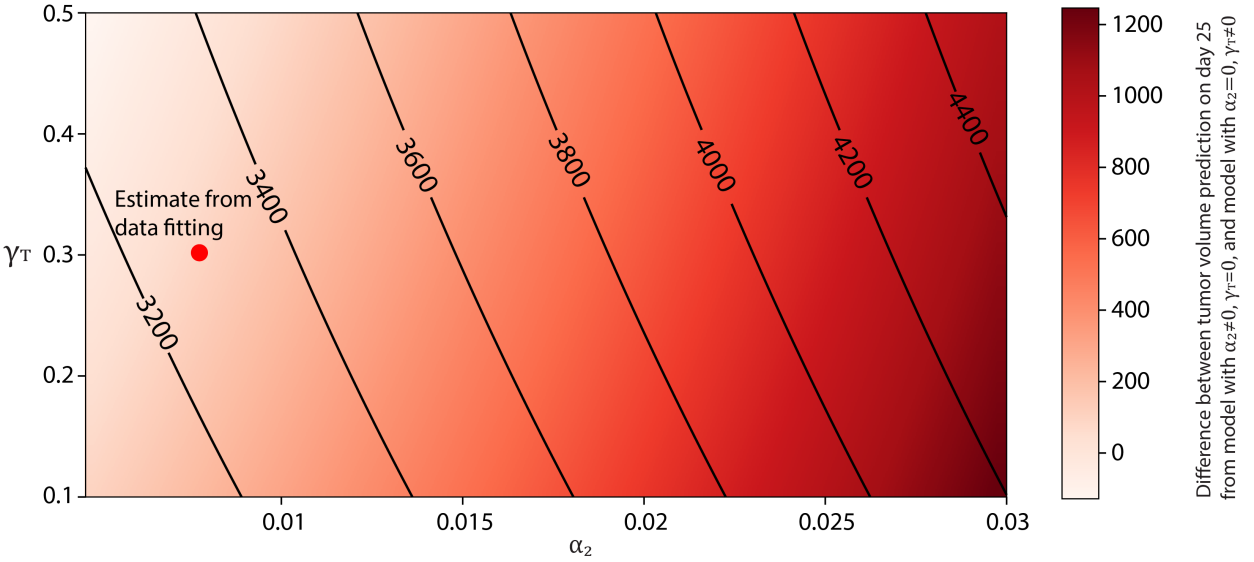

FIGURE 7. Heatmap showing the difference between tumor volume in mice on day 25 predicted from model with $\alpha_2 \in [0.001, 0.03]$ and $\gamma_T = 0$ and volume in mice on day 25 predicted from model with $\alpha_2 = 0$ and $\gamma_T \in [0.1, 0.5]$. The red dot represents the difference between the model with $\alpha_2 = 0.007\,74\,\mathrm{d}^{-1}, \gamma_T = 0$ and the model with $\alpha_2 = 0\,\mathrm{d}^{-1}, \gamma_T = 0.3018$, indicating that FGFR3 mutation have an almost equal effect on both tumor proliferation and survival in the experimental design. The contour plot shows the prediction of tumor volume on day 25 at the different pairs of α_2 and γ_T in the ranges $[0.001, 0.03]$ and $[0.1, 0.5]$, respectively.

4 Treatment Results

We next turn to the question of understanding the effects of therapy on the tumor reduction. Specifically, in this section we simulate the model with immune checkpoint and FGFR3 targeted therapy alone and in combination. The dosing schedule for the therapies are presented in Figure 8 – anti-FGFR3 therapy is administered every day starting from day 7 through day 25 except on days 12, 13, 19, and 20 (these days are regarded as off-days) and anti-PD-L1 antibody is administered every 3 days starting on day 7 (except on the off-days).

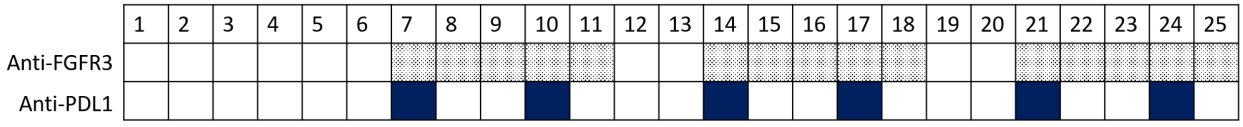

FIGURE 8. Dosing schedule of anti-FGFR3 and anti-PD-L1 monotherapies.

4.1 Treatment with anti-PD-L1 Antibody Alone

In order to study the effect of monotherapy with an anti-PD-L1 immunotherapeutic agent, we calibrated Equations (1), (3), and (9)) with the experimental data for tumor cells without the FGFR3 mutation in mice (Figure 9A). In the experiments that generated this data, doses of 100 µg anti-PD-L1 therapeutic agent with a half-life of 48 hours was administered to mice via intraperitoneal injection using the baseline schedule in Figure 8. We used this data to estimate the drug dissociation constant (K_D) and the depletion rate of anti-PD-L1 antibodies through binding to PD-L1 (μ_{LA}). These results are shown in Fig 9A. With the model now calibrated to data where the FGFR3 mutation is absent, we turn to validating the model with data where the FGFR3 mutation is active. Specifically, to accomplish this validation step, we directly compared (i.e., no additional parameter fitting) the model simulations with the experimental data of anti-PD-L1 therapy against FGFR3-mutant tumor cells (Figure 9B). The result shows an excellent correlation between the model and the data without the need for parameter tuning.

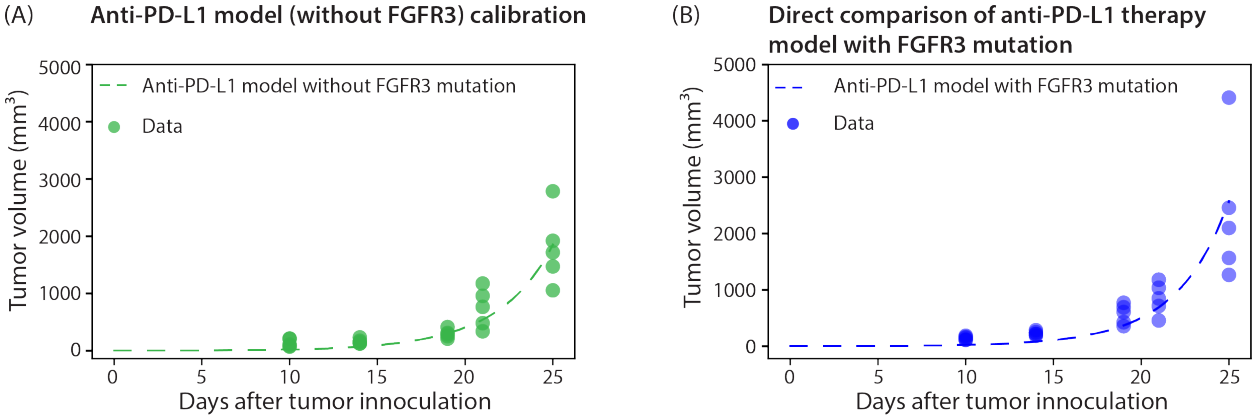

FIGURE 9. (A) Anti-PD-L1 therapy model calibration to experimental data of anti-PD-L1 therapy on tumor cells without FGFR3 mutation in mice to estimate $K_D = 0.1005\,\text{nM}$, $\mu_{LA} = 2.6611 \times 10^{-5}\,\text{d}^{-1}$. (B) The estimated parameters are used to simulate the anti-PD-L1 therapy model with FGFR3 mutation, and directly compared with the corresponding data in mice. Parameter values used are given in Tables 2 and 4.

In Figure 10, the model output from Figures 9A and B is compared to the corresponding models without anti-PD-L1 therapy. The larger gap in 10A compared to 10B shows that mice without FGFR3 mutation receive more benefit from anti-PD-L1 therapy compared to mice with FGFR3

mutation.

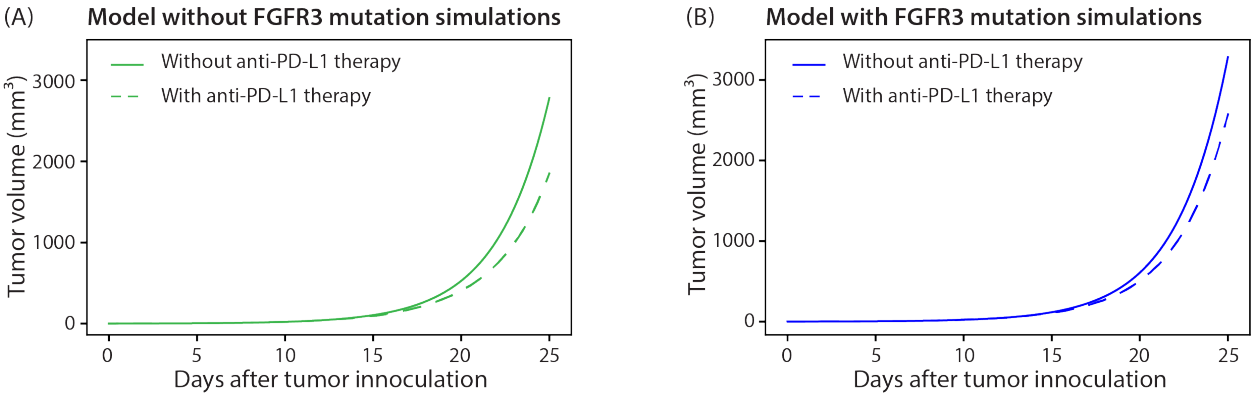

FIGURE 10. Comparison of models with anti-PD-L1 therapy. Results in (A) and (B) show that mice without FGFR3 mutation receive more benefit from anti-PD-L1 therapy compared to mice with FGFR3 mutation. Parameter values used are given in Tables 2 and 4.

4.2 Treatment with anti-FGFR3 Inhibitor Alone

Next we investigate targeted therapy against the FGFR3 receptor using the dosing schedule in Figure 8. To estimate rogaratinib pharmacokinetic parameters, we fit a three-compartment model for rogaratinib bio-distribution (described in Appendix B) to experimental data of rogaratinib plasma concentration in mice [17]. Using these parameter values, we simulated (see Figure 11) FGFR3 mutant tumor response to the following doses of rogaratinib: 25 mg/kg QD (once a day), 25 mg/kg BID (twice a day), 50 mg/kg QD, and 75 mg/kg QD using the dosing schedule in Figure 8. It is clear from Figure 11 that the various doses of anti-FGFR3 drugs do not have substantial impacts on the tumor volume. Also, the effect sizes of the doses are approximately equal. These results are not surprising since this tumor cell line is not dependent on the FGFR3 activating mutation–which was exogenously introduced to study its impact on anti-PD-L1 therapy as shown in Fig 10–for enhanced tumor growth.

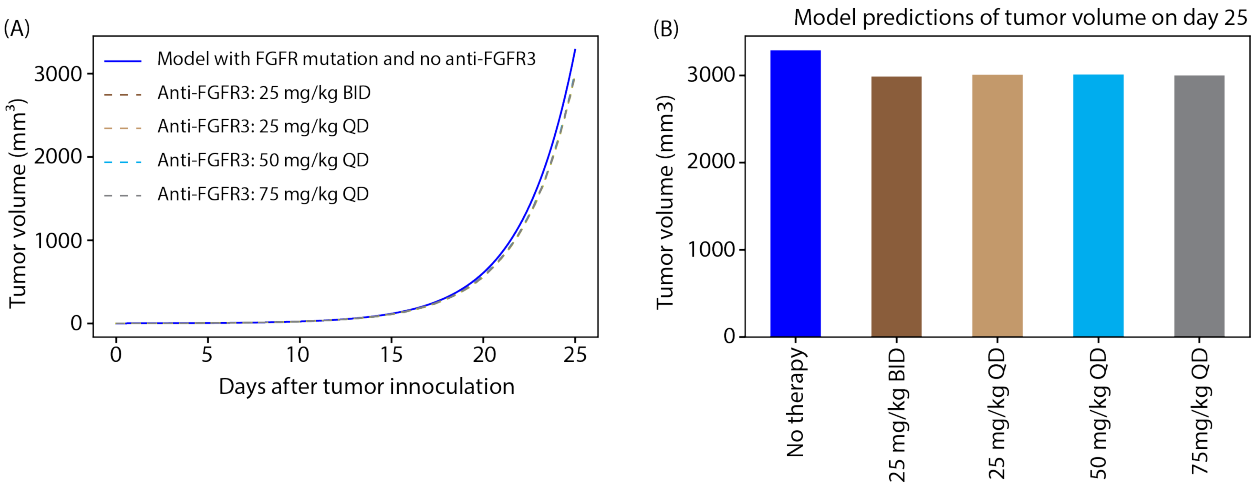

FIGURE 11. Simulation of anti-FGFR3 therapy model with FGFR3 mutation with no treatment, 25 mg/kg QD (once a day), 25 mg/kg BID (twice a day), 50 mg/kg QD, and 75 mg/kg QD of rogaratinib using the dosing schedule in Figure 8. (B) Model prediction of tumor volume on day 25 in mice. Parameter values used are given in Tables 2-4.

4.3 Treatment with Combination Therapy

We simulated the model to predict the effect of combining anti-FGFR3 and anti-PD-L1 therapies on tumor cells with FGFR3 mutation in mice (using the dosing schedule in Figure 8 with co-treatment on days 7, 10, 14, 17, 21 and 24). The result is shown in Figure 12, along with the impact of anti-FGFR3 therapy only and anti-PD-L1 therapy only. Our model predictions show that the effect of each therapy is approximately additive when combined, and combination therapy reduces the tumor volume on day 25 by 33.3% compared to 21.9% in the case of anti-PD-L1 therapy only. Similar results were obtained when the anti-PD-L1 therapy is combined with either 25 mg/kg QD, 25 mg/kg BID or 50 mg/kg QD dose of rogaratinib (results not shown).

We further simulated the model with a wider range of the parameters that govern FGFR3 impact on proliferation ($\alpha_2 \in [0.001, 0.03]$) and survival ($\delta_1 \in [0.1, 0.5]$) to compare the effectiveness of anti-PD-L1 and anti-FGFR3 monotherapies when the influence of the FGFR3 mutation on tumor growth varies. The results depicted in Figure 13 show that for some combinations of α_2 and γ_T, especially in the region where the FGFR3 pathway has significant impact on tumor growth, the targeted therapy outperforms the immune checkpoint monotherapy (this result also shows the possible significant impact of anti-FGFR3 monotherapy on FGFR3 overexpressing cancers). It is also important to

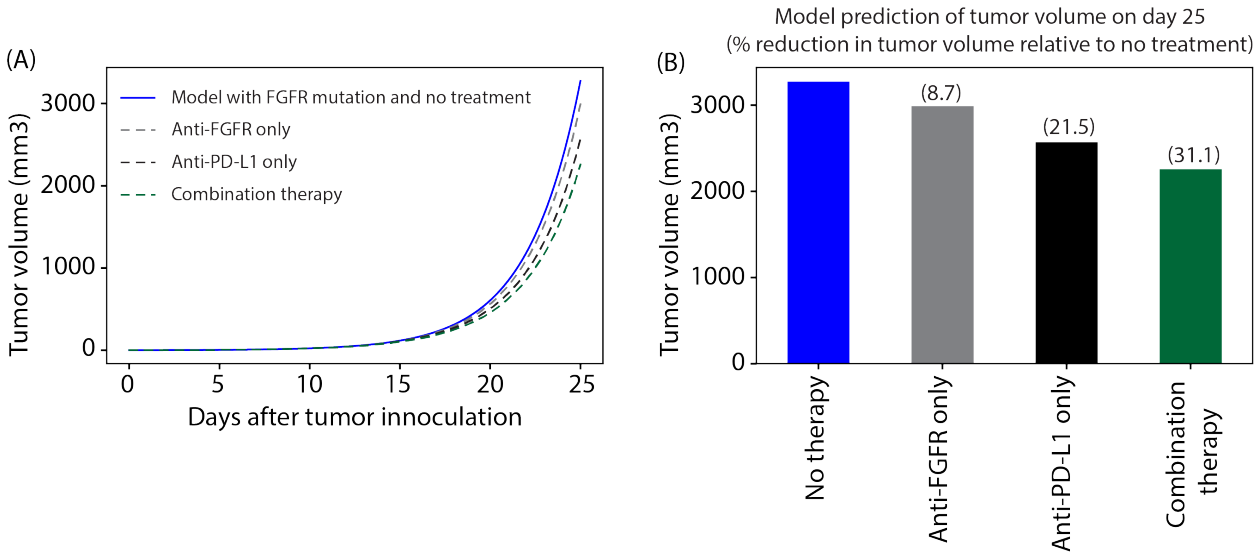

FIGURE 12. (A) Simulation of model with FGFR3 mutation with no therapy (blue), anti-FGFR3 therapy only (gray), anti-PD-L1 therapy only (black) and combination therapy (green). (B) Model prediction of tumor volume on day 25 in mice. Parameter values used are given in Tables 2-4.

note, by comparing Figure 12B to Figure 13BII, that the efficacy of combination therapy can be significantly increased in parameter ranges where there is a substantial increase in the effectiveness of rogaratinib while anti-PD-L1 therapy retains its efficacy.

4.4 Kaplan-Meier Survival Analysis

Kaplan-Meier survival analysis is used to measure the fraction of subjects living for a certain amount of time after treatment in an experiment or clinical trial [29]. To further estimate the effects of anti-FGFR3 monotherapy, anti-PD-L1 monotherapy, and combination therapies on tumor with FGFR3 mutation using the baseline dosing schedule in Figure 8, we carried out a Kaplan-Meier analysis by measuring the fraction of mice, S_t, surviving at time t using the formula below:

$$S_t = \frac{N - N_{TV \geq 2000 mm^3, t}}{N}, \tag{12}$$

where N is the total number of mice and $N_{TV \geq 2000 mm^3, t}$ is the number of mice that did not survive (i.e., mice with tumor volume (TV) above or equal to the survival threshold ($2000\,\mathrm{mm}^3$)) at time t. We generated 50 mice by randomly sampling the sensitive parameters ($\alpha_1, \delta_T, \alpha_2$, and γ_T) within

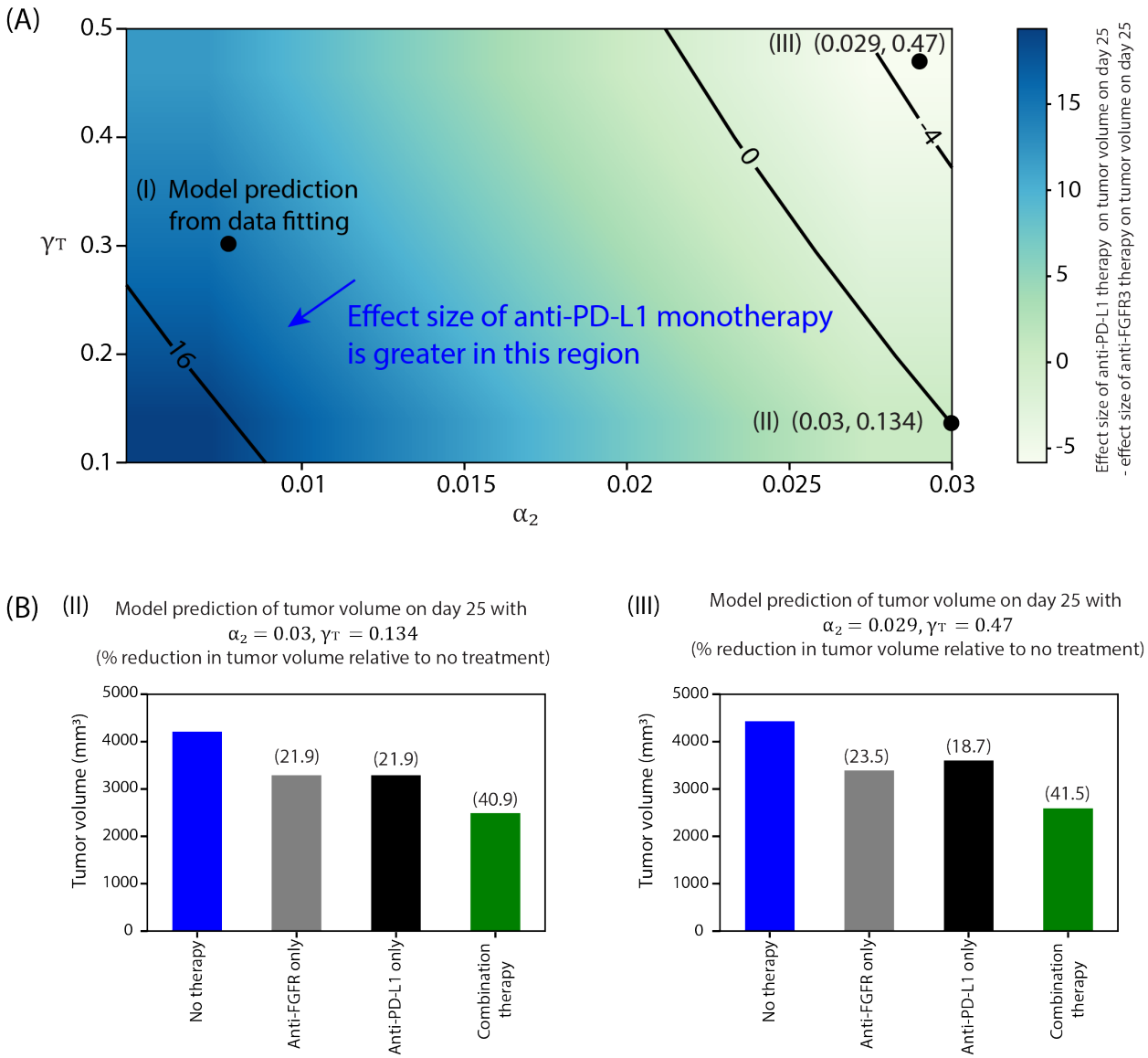

FIGURE 13. (A) A heatmap showing the difference in effect size of anti-PD-L1 and anti-FGFR3 therapies on day 25 on tumor with FGFR3 mutation. The black dot (i) indicate an example where anti-PD-L1 therapy has larger effect size than anti-FGFR3 therapy (the values for the effect sizes are shown in Figure 12B) (B) Prediction of tumor volume and effect size of anti-PD-L1 monotherapy, anti-FGFR3 monotherapy, and combination therapy using (ii) $\alpha_2 = 0.03\,\mathrm{d}^{-1}$ and $\gamma_T = 0.134$ where the effect size of anti-PD-L1 and anti-FGFR3 are approximately equal; and (iii) $\alpha_2 = 0.029\,\mathrm{d}^{-1}$ and $\gamma_T = 0.47$ where anti-PD-L1 therapy has lesser effect size than anti-FGFR3 therapy. The arrow indicates the direction of increasing relative strength of anti-PD-L1 monotherapy.

their ranges of values given in Table 2. In particular, we generated normal sampling distributions for practically identifiable parameters (α_1 and α_2) using their respective mean and standard deviation

and uniform sampling distributions for practically non-identifiable parameters (δ_1 and γ_T). The simulation was repeated for five stochastic realizations. The result depicted in Figure 14 shows that 78 – 96% of the mice treated with combination therapy survived on day 25 compared to mice treated with anti-PD-L1 monotherapy (62 – 76%), anti-FGFR3 monotherapy (28 – 42%) or untreated mice (10 – 20%). Since the values for the FGFR3-dependent parameters are within the region where anti-PD-L1 monotherapy has more effect size than anti-FGFR3 monotherapy (Figure 13A), we expect that more mice would survive when treated with anti-PD-L1 therapy.

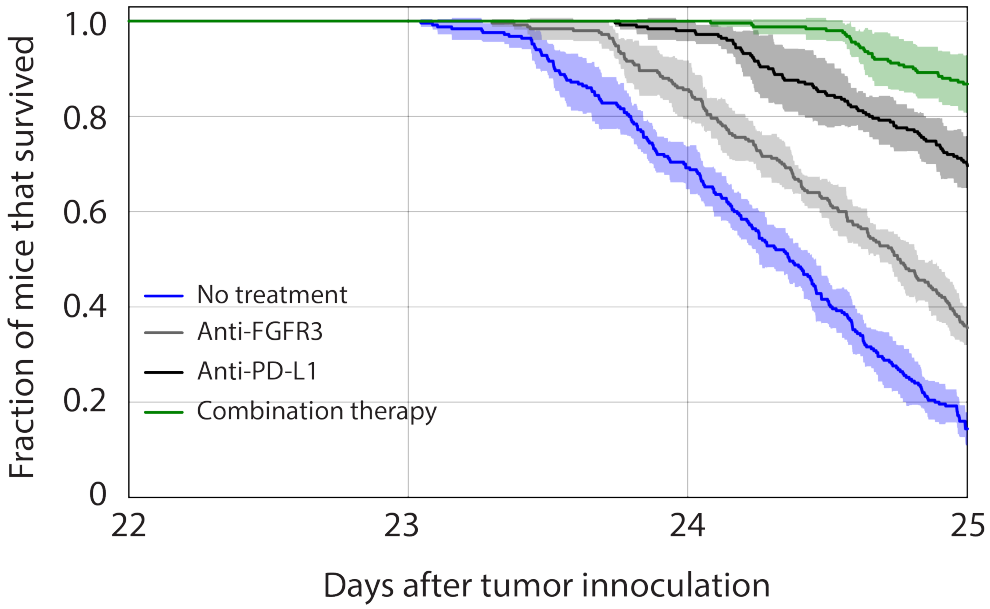

Mean number of mice at risk			
No treatment	50	34	7
Anti-FGFR3	50	42	18
Anti-PD-L1	50	49	34
Combination therapy	50	50	43

FIGURE 14. Kaplan-Meier survival analysis showing the fraction (mean ± SD) of mice that survived with no treatment (blue), anti-FGFR3 monotherapy (gray), antiPD-L1 monotherapy (black) and combination therapy (green). Parameter values used are in Tables 2-4 with normal distribution of α_1 (with mean = $0.337\,\mathrm{d}^{-1}$ and standard deviation = $0.0034\,\mathrm{d}^{-1}$), normal distribution of α_2 (with mean = $0.007\,74\,\mathrm{d}^{-1}$ and standard deviation = $0.0016\,\mathrm{d}^{-1}$), uniform distributions of δ_1 and γ_T within their range of values in Table 2

Figure 15 shows the distribution of parameters associated with the mice that survived until day

25 in the Kaplan-Meier survival analysis. These results show that the surviving mice are characterized by high CTL-induced death rate (δ_1) (i.e., slow-growing tumor cells). In particular, the only untreated mice that survived until day 25 had a CTL-induced death rate above $1.9 \times 10^{-7}\text{cell}^{-1}\,\text{d}^{-1}$; those treated with anti-FGFR3 monotherapy needed at least a value of $1.6 \times 10^{-7}\text{cell}^{-1}\,\text{d}^{-1}$ (with one exception). Even anti-PD-L1 monotherapy and combination therapy needed δ_1 to exceed $1.3 \times 10^{-7}\text{cell}^{-1}\,\text{d}^{-1}$ to give at least even odds for the mice to survive until day 25.

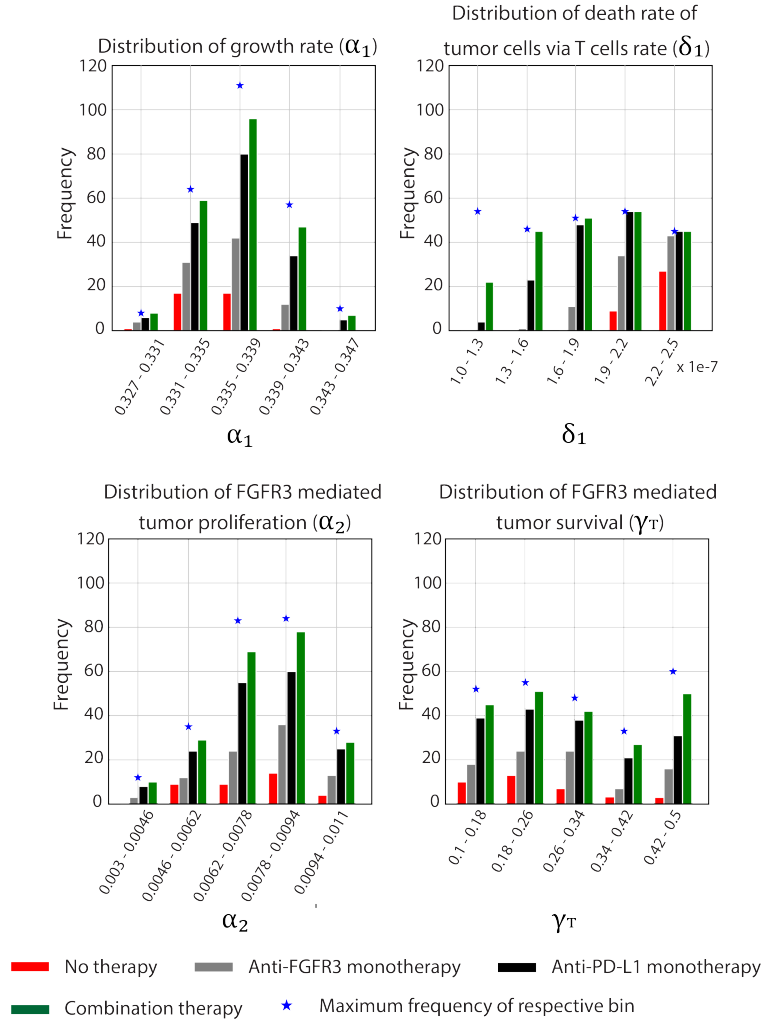

FIGURE 15. Distribution of sensitive parameters related to mice that survived on day 25 of survival analysis with different therapeutic conditions. The distances between each bar and the maximum frequency represent the distribution of mice that did not survive in the Kaplan-Meier analysis.

4.5 Dosing Schedules

Next, we use the model to determine how best to administer anti-PD-L1 and anti-FGFR3 targeted therapies. To determine the most favorable combinations and to investigate the potential synergy between anti-PD-L1 and anti-FGFR3 therapies in mice with FGFR3 mutation, we simulate different dose-scheduling for anti-FGFR3 and anti-PD-L1 therapies (Figure 16).

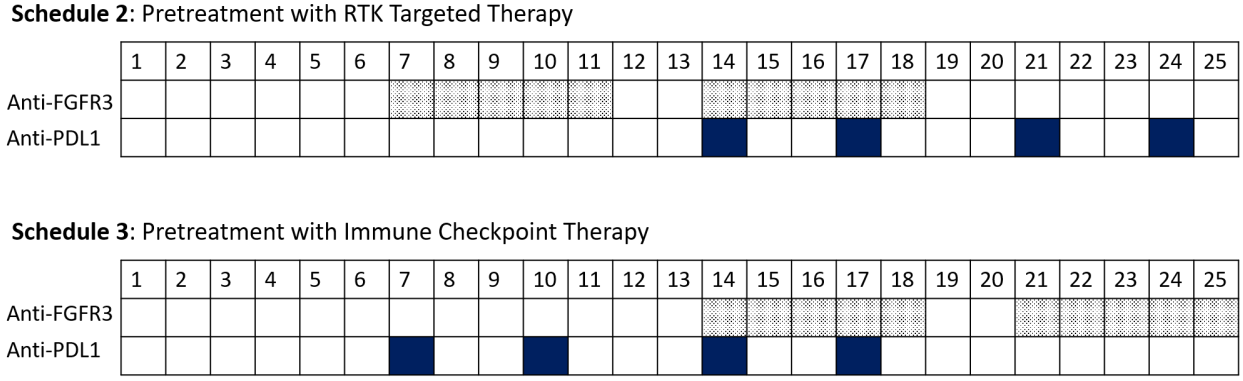

FIGURE 16. Dosing schedule of pretreatment with anti-FGFR3 therapy and pretreatment with anti-PD-L1 therapy.

In these simulations, we considered treatments of tumor cells with FGFR3 mutation with a total of 10 doses of 75 mg/kg QD of rogaratinib and 4 doses of 100 µg of anti-PD-L1 antibody using the dosing schedules 2 and 3 shown in Figure 16 (compared to 15 doses of anti-FGFR3 and 6 doses of anti-PD-L1 in the dosing schedule (baseline schedule) in Figure 8).

The ultimate goal is to determine the optimal dosing strategy that minimizes tumor growth while also minimizing the amount of drug administered. The tumor is either pretreated with anti-FGFR3 therapy or pretreated with anti-PD-L1 therapy as shown in Figure 17. The results depicted in Figures 17 show that the pretreatment of tumors with anti-PD-L1 therapy (Schedule 3) is more effective than pretreatment of tumors with anti-FGFR3 therapy (Schedule 2). This result persists throughout the $\alpha_2 - \gamma_T$ parameter space, even in regions where anti-FGFR3 monotherapy greatly outperforms immune checkpoint monotherapy (result not shown). It is also important to note that that the outcomes for Schedule 3 are comparable to those from the baseline schedule of co-treatment, which administers five additional doses of therapy.

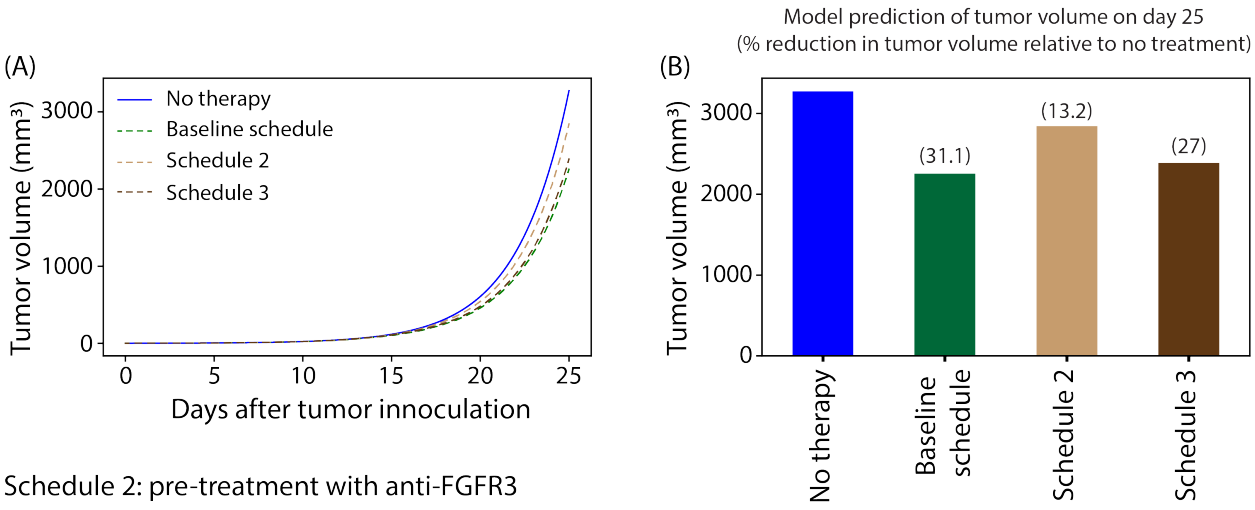

Schedule 2: pre-treatment with anti-FGFR3

Schedule 3: pre-treatment with anti-PDL1

FIGURE 17. Simulation showing effect size of the different dosing schedules (A) Simulation of model with FGFR3 mutation with no therapy (blue), treatment with baseline combination therapy (green), pretreatment with anti-FGFR3 therapy, and pretreatment with anti-PD-L1 therapy. (B) Model prediction of tumor volume on day 25 in mice. Parameter values used are given in Tables 2-4.

5 Discussion

Until recently, systemic chemotherapy was the only recourse for people suffering from bladder cancer, and outcomes remained discouraging as many patients either fail to respond to treatment or suffer recurrent disease within 5 years [30, 31]. After nearly four decades of little progress, immunotherapy with checkpoint inhibitors (PD-L1 and PD-1) has fundamentally shifted the treatment paradigm of bladder cancer [31]. At the same time, advances in the understanding of the molecular biology of bladder cancer has led to the identification of molecular pathways, such as FGFR3 signaling, upon which new therapeutic approaches can be targeted [32]. In this paper, we developed an experimentally-validated mathematical model for the dynamics of bladder cancer growth and response to receptor tyrosine kinase (RTK) targeted therapy alone and in combination with an immune checkpoint inhibitor (ICI). This model is the first of its kind in that it incorporates the molecular details of an FGFR3 mutation that initiates signaling via ligand-independent dimerization to enhance tumor cell proliferation and survival. Our model formulation allows us to track the fraction of active FGFR3 dimers and to use this quantity to augment the rates of tumor cell

division and tumor cell death, which is mediated by cytotoxic T cells. A second important feature of our model is that it explicitly accounts for the formation of PD-1/PD-L1 complexes that inhibit T cell proliferation and activation.

The model is carefully calibrated and validated with experimental measures of tumor volume with and without the FGFR3 mutation. In an attempt to identify which FGFR3-mediated effect has more impact on tumor growth, we computed the difference between the tumor volume when FGFR3 only impacts the tumor cell proliferation rate and the tumor volume when FGFR3 only impacts tumor cell survival. The results suggest that FGFR3 mutation can lead to increased tumor volume due primarily to either proliferation or survival effects–depending on the relative strengths of these signaling pathways, i.e. the parameters. However, the proliferation effect is more influential across a larger region of parameter space. Interestingly, for our estimated parameter values, the effects of FGFR3 on proliferation and survival are nearly equal.

Based on the mechanisms of action of an immune checkpoint inhibitor targeting PD-L1 and a tyrosine kinase inhibitor targeting FGFR3 (rogaratinib), we extended our model to evaluate the impact of these therapies alone and in combination. Simulations of anti-PD-L1 therapy showed that tumors with FGFR3 mutation are more susceptible to anti-PD-L1 therapy than wild type FGFR3 tumors. This effect is likely independent of FGFR3 effects on intrinsic tumor growth and survival, since both cell lines grow essentially at the same rate in the presence or absence of FGFR3 activating mutations. These results are in line with our reported experimental data and suggest that the FGFR3 mutation can impact the effectiveness of anti-PD-L1 therapy. Furthermore, the experiments described here use a tumor cell line that is not dependent on the FGFR3 activating mutation, which was exogenously introduced. Thus, we did not expect the FGFR3 activating mutation to have a significant impact on tumor growth. Our anti-FGFR3 monotherapy model simulations clearly show that this is indeed the case for four different doses of rogaratinib. However, when we simulated a wider range of the parameters that govern FGFR3 impact on proliferation and survival, we saw that for realistic values of α_2 and γ_T, anti-FGFR3 therapy can not only have substantial impact on tumor reduction, targeted therapy can actually outperform anti-PD-L1 monotherapy.

Despite the slight impact of rogaratinib monotherapy on tumor cells with FGFR3 mutation when baseline parameters are used, our model simulations show that its combination with anti-PD-L1 therapy increases the effect size of the anti-PD-L1 therapy on tumor cells with the FGFR3 mutation. That is, while anti-PD-L1 antibody loses efficacy when the FGFR3 mutation is active, anti-PD-L1 antibody impact on tumor reduction is recovered when combined with a drug that targets FGFR3. In fact, Kaplan-Meier survival analysis showed that when mice with FGFR3 mutant bladder cancer are treated with combination therapy, they have a much higher probability of surviving to day 25 compared to mice treated with either monotherapy. We also found that there are parameter ranges for of α_2 and γ_T where there is a significant increase in tumor reduction due to rogaratinib and only a small decrease in tumor reduction due to immune checkpoint therapy, and this leads to a substantial increase in the efficacy of combination therapy.

In an attempt to find the most effective way of delivering combinations of these two therapies , we simulated two different dose-scheduling regimens for rogaratinib and an immune checkpoint inhibitor targeting PD-L1. We compared outcomes of these strategies to each other and to our baseline dose schedule of co-treatment, which administers five additional doses of rogaratinib. Our results show that pretreatment with anti-PD-L1 therapy leads to greater tumor reduction than pretreatment with anti-FGFR3 therapy. Interestingly, even in parameter regimes where anti-FGFR3 monotherapy greatly outperforms immune checkpoint monotherapy, the model predicts that it is still better to pretreat with the anti-PD-L1 drug. Furthermore, our baseline schedule of co-treatment performs only slightly better, with five additional doses of anti-PD-L1 therapy, than pretreatment with anti-PD-L1 therapy. This result suggests that some patients may benefit more from pretreatment with anti-PD-L1 because fewer drug doses can be used to achieve similar outcomes. These findings have direct clinical relevance given that anti-FGFR3 therapy is currently FDA approved, but it remains unknown whether it is best employed prior to or after anti-PD-L1 immunotherapy.

This modeling study not only quantifies the influence of the FGFR3 mutation on bladder cancer growth; it also predicts various outcomes for RTK and ICI mono- and combination therapy. In the current model formulation, we are considering the total amount of FGFR3 monomers in the system and allowing all monomers to interact with each other. The resulting dimerization of monomers

allows us to quantify the temporal changes in fractional occupancy of active FGFR3 dimers in the system and their impact on tumor growth dynamics. In future iterations of the model, we could relax these assumptions and reformulate the model so that FGFR3 monomers only interact with other monomers on the same cell. We are currently modifying this model to describe different mechanisms of immune cell kill. We will also extend the model to include the impact of spatial dynamics by translating this system of ordinary differential into an agent-based modeling framework. Continued computational modeling of bladder cancer therapy can potentially lead to patient specific optimization of combination of anti-FGFR3 with anti-PD-L1 treatments.

Appendix

A. Formulation for PD-1/PD-L1 Complexes, Q

Following [12], the molar concentration of PD-L1 (L) within the tumor microenvironment consists of the amount of free PD-L1 and the amount of PD-L1 bound to the drug,

$$L = L_{free} + L_{bound},$$

with $L = \rho_L(Y + \epsilon T)$. We consider the following reaction:

$$P_D + L_{free} \underset{\delta_Q}{\overset{\alpha_{PL}}{\rightleftharpoons}} Q,$$

Following [10, 12, 13, 16], we assume that the association and dissociation of Q are fast, so applying a quasi-steady state argument, we can approximate Q using the equation:

$$Q = \frac{\alpha_{PL}}{\delta_Q} P_D L_{free} = \frac{\alpha_{PL}}{\delta_Q} P_D (L - L_{bound}). \tag{A-1}$$

We also considered the following reaction:

$$L_{free} \underset{k_{-1}}{\overset{k_{+1}}{\rightleftharpoons}} L_{bound},$$

where k_{+1} and k_{-1} are the association and dissociation rates of L_{bound}. By the law of mass action and assuming the process is at equilibrium [12],

$$\begin{aligned} \frac{dL_{bound}}{dt} &= k_{+1} L_{free} A - k_{-1} L_{bound} = 0 \\ L_{bound} &= \frac{k_{+1}}{k_{-1}} L_{free} A = \frac{k_{+1}}{k_{-1}} (L - L_{bound}) A \\ L_{bound} &= \frac{A}{A + K_D} L \end{aligned} \tag{A-2}$$

where $K_D = \dfrac{k_{-1}}{k_{+1}}$ (i.e., the dissociation constant of the PD-L1/anti-PD-L1 complex). Thus, by substituting Equation (A-2) into Equation (A-1), we derived the following expression for Q, given

by:

$$Q = \frac{\alpha_{PL}}{\delta_Q} P_D L \left(1 - \frac{A}{A + K_D}\right)$$

Finally, we choose the following functional form for $F(Q)$ defined by

$$F(Q) = \frac{1}{1 + \dfrac{Q}{K_{TQ}}} \qquad \equiv \qquad F(P, L, A) = \frac{1}{1 + \dfrac{P_D L}{K_{YQ}} \left(1 - \dfrac{A}{A + K_D}\right)} \tag{A-3}$$

where $K_{YQ} = \dfrac{\delta_Q}{\alpha_{PL}} K_{TQ}$ (described in Table 2) [10, 12, 13, 16]. In order to achieve agreement between the units for A and K_D in Equation A-3, we converted the dosage of anti-PD-L1 in the experiment from µg to nmol/L using the following formula:

$$c\,(\text{nmol/L}) = \frac{m\,(\mu\text{g})}{V\,(\text{L}) \times \text{molar mass}\,(\mu\text{g/nmol})},$$

where V is the carrying capacity of tumor volume without FGFR3 mutation ($4000\,\text{mm}^3 = 0.004\,\text{L}$), molar mass $= 1.5 \times 10^5\,\text{g/mol} = 1.5 \times 10^2\,\mu\text{g/nmol}$, so that $100\,\mu\text{g}$ of anti-PD-L1 is equivalent to $166.67\,\text{nmol/L}$ of anti-PD-L1.

B. Pharmacokinetics of anti-FGFR3 (rogaratinib)

We developed a compartmental model to describe the pharmacokinetic profile of rogaratinib in the plasma. The pharmacokinetic model is given as follows, where $G(t), C_S(t)$, and $C_P(t)$ represents the concentration of the drug in the gut, central, and peripheral compartments, respectively:

$$\begin{aligned} \frac{dG}{dt} &= k_a G \\ \frac{dC_S}{dt} &= F k_a G - k_{12} C_S + k_{21} C_P - k C_S \\ \frac{dC_P}{dt} &= k_{12} C_S - k_{21} C_P \end{aligned} \tag{B-1}$$

where k_a is the first-order absorption rate constant, k is the elimination rate constant, F is the bioavailability of the drug that accounts for the fraction of dose that reaches the central compartment, and k_{12} and k_{21} are distribution rate constants from the central compartment to the peripheral

compartment and vice versa, respectively. The pharmacokinetic parameters are estimated by fitting the analytical solution of the central compartment, ($C_S(t)$) to the experimental data of the oral administration of rogaratinib described in [17]. The best fit values and fitting are given in Table Table 3 and Figure 18, respectively.

TABLE 3. Best fit pharmacokinetic parameter of rogaratinib for PK model (B-1)

Parameter	**Description**	**Best fit values**			**Reference**
		75 mg/kg	50 mg/kg	25 mg/kg	
k_a	Absorption rate	$0.4815\,h^{-1}$	$0.3597\,h^{-1}$	$0.4942\,h^{-1}$	Estimated
F	Bioavailabilty	$0.42\,h^{-1}$	$0.42\,h^{-1}$	$0.42\,h^{-1}$	[19]
k_{12}	Plasma-Tissue transfer rate	$577.44\,h^{-1}$	$423.11\,h^{-1}$	$47.915\,h^{-1}$	Estimated
k_{21}	Tissue-Plasma transfer rate	$1.2478\,h^{-1}$	$2.6785\,h^{-1}$	$0.2864\,h^{-1}$	Estimated
k	Elimination rate	$193.53\,h^{-1}$	$202.95\,h^{-1}$	$309.15\,h^{-1}$	Estimated

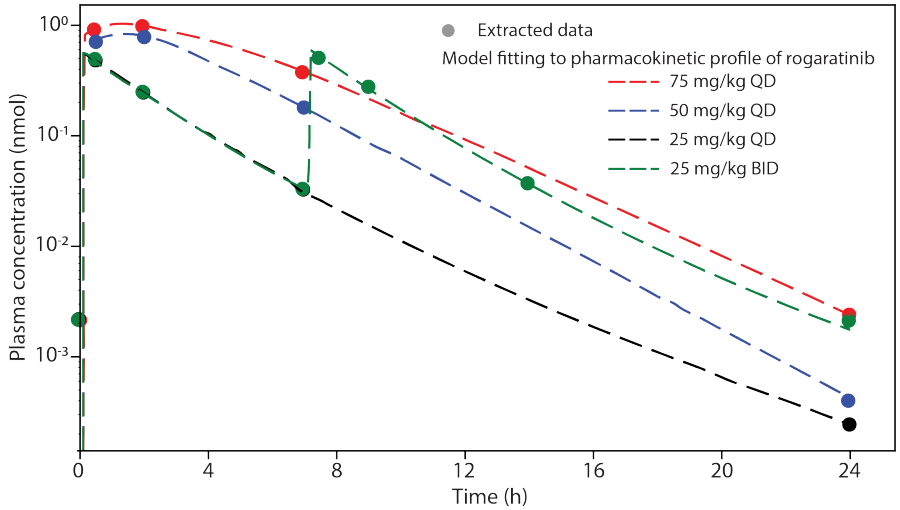

FIGURE 18. Time profiles of single-dose of 75 mg/kg QD (red dashed line), 50 mg/kg QD (blue dashed line), 25 mg/kg QD (black dashed line) and 25 mg/kg BID (green dashed line) of rogaratinib in plasma. The best fit of model is plotted together with experimental data of rogaratinib in mice described in [17]. Parameter values used are given in Tables 2-4.

C. Model equations related to treatment with anti-FGFR3 (rogaratinib)

The system of equations governing the dynamics of the FGFR3 monomers and dimers (see Figure 19) in the tumor cell in the presence of rogaratinib is given by,

$$\begin{aligned}
\frac{dR_F}{dt} &= -2k_f R_F^2 + 2k_r D_A + 2k_p(D_A + D_C^C + D_A^C) + R_T P(T,\phi_D) - k_{c,on}^R C R_F + k_{c,off}^R R_F^C \\
&\quad - \frac{R_F}{\Sigma} R_T D(T,Y,\phi_D^C), \\
\frac{dD_A}{dt} &= k_f R_F^2 - k_r D_A - k_p D_A - k_{c,on}^D C D_A + k_{c,off}^D D_A^C - \frac{D_A}{\Sigma} R_T D(T,Y,\phi_D^C), \\
\frac{dC}{dt} &= k_{12} C_1 - k_{21} C - k_{c,on}^R C R_F + k_{c,off}^R R_F^C - k_{c,on}^D C D_A + k_{c,off}^D D_A^C, \\
\frac{dR_F^C}{dt} &= k_{c,on}^R C R_F - k_{c,off}^R R_F^C - 2k_f (R_F^C)^2 + 2k_r D_C^C - \frac{R_F^C)}{\Sigma} R_T D(T,Y,\phi_D^C), \\
\frac{dD_C^C}{dt} &= k_f (R_F^C)^2 - k_r D_C^C - k_p D_C^C - \frac{D_C^C}{\Sigma} R_T D(T,Y,\phi_D^C,) \\
\frac{dD_A^C}{dt} &= k_{c,on}^D C D_A - k_{c,off}^D D_A^C - k_p D_A^C - \frac{D_A^C}{\Sigma} R_T D(T,Y,\phi_D^C),
\end{aligned} \tag{C-1}$$

where R_F, D_A, R_F^C, and D_A^C represent the free FGFR3 monomers, active dimers, monomer/rogaratinib complex, and active dimer/rogaratinib complex respectively (see Figure 2 for the flowchart of the mechanism of action of rogaratinib). The monomer/rogaratinib complexes dimerize to form D_C^C, and C represents the concentration of rogaratinib in the tumor microenvironment. As an anti-FGFR3 drug, we assumed that rogaratinib binds to the kinase region of FGFR3 monomers (R_F) and active dimers (D_A) on tumor cells at rates $k_{c,on}^R$ (to form monomer/rogaratinib complex (R_F^C)) and $k_{c,on}^D$ (to form active dimer/rogaratinib complex (D_A^C)). These complexes dissociate at rates $k_{c,off}^R$ and $k_{c,off}^D$, respectively. Furthermore, we assume that rogaratinib drug does not affect dimerization, dissociation, and internalization, thus, the monomer/rogaratinib complex (R_F^C) dimerizes at a rate k_f to form D_C^C which can either dissociate at a rate k_r, internalized at a rate k_p. We assumed that upon internalization, both monomer/rogaratinib and active dimer/rogaratinib complexes are recycled at a rate k_p, leaving behind the drug, to reproduce FGFR3 monomers (R_F). The term ϕ_D^C is the fractional occupancy of active dimer on a tumor cell with anti-FGFR3 and $\Sigma = R_F + 2D_A + R_F^C + 2D_C^C + 2D_A^C$. The flowchart and parameter values for model (C-1) are given in Table 4 and Figure 19, respectively.

The underlying assumptions for this equation are (i) the tumor resides in a pharmacokinetic compartment of its own; (ii) the binding rates are the same, independent of cell type; (iii) rogaratinib is transferred into the tumor from the systemic circulation at the same rate as the peripheral tissue, k_{12}; and (iv) the tumor volume is negligible compared to the volume of a mouse; therefore the amount of the drug leaking into the bloodstream (at the rate k_{21}) will not affect the concentration of free rogaratinib in the systemic circulation. Furthermore, the formulation of the model (C-1) assumes that the total number (converted to nmol using molecular weight) of receptors per tumor cell R_T remains constant. Thus, we can ensure that the model equations do conserve FGFR3 by considering the sum:

$$\frac{dR_F}{dt} + 2\frac{dD_A}{dt} + \frac{dR_F^C}{dt} + 2\frac{dD_C^C}{dt} + 2\frac{dD_A^C}{dt} = \frac{d\Sigma}{dt} = R_T\left(P(T,\phi_D^C) - D(T,Y,\phi_D^C)\right) = R_T\frac{dT}{dt}.$$

Therefore, upon integration, we have $\Sigma = R_T \times T$.

TABLE 4. Parameter Values Related to anti-FGFR3 and anti-PD-L1 Therapy

Parameter	**Description**	**Baseline Value**	**Units**	**Reference**
Anti-FGFR3 related				
$k_{c,on}^R$	Rogaratinib-FGFR3 monomer association rate	1.28×10^5	$\text{nmol}^{-1}\,\text{d}^{-1}$	[17]
$k_{c,off}^R$	Rogaratinib-FGFR3 monomer dissociation rate	95.04	d^{-1}	[17]
$k_{c,on}^D$	Rogaratinib-FGFR3 dimer association rate	1.28×10^5	$\text{nmol}^{-1}\,\text{d}^{-1}$	[17]
$k_{c,off}^D$	Rogaratinib-FGFR3 dimer dissociation rate	95.04	d^{-1}	[17]
Anti-PD-L1 related				
μ_{LA}	Anti-PD-L1 depletion via binding to PD-L1	2.66×10^{-5}	$\text{nM}^{-1}\,\text{d}^{-1}$	Estimated
δ_A	Anti-PD-L1 natural degradation rate	0.3466	d^{-1}	Estimated
K_D	PD-L1-Anti-PD-L1 dissociation rate	0.1005	nM	Estimated

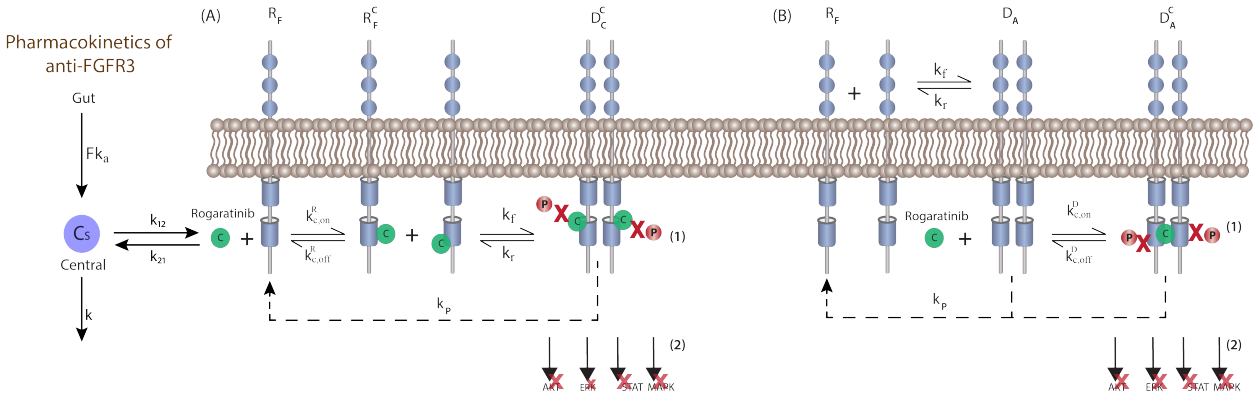

FIGURE 19. Flowchart of rogaratinib as anti-FGFR3 treatment. (A) Rogaratinib drug associate with FGFR3 monomer on tumor cells at a rate $k^R_{C,on}$ to form R^C_F and dissociate at a rate $k^R_{C,off}$. R^C_F dimerize at a rate k^C_f to form D^C_C which can either dissociate at rate k_r, or internalize and recycled into FGFR3 monomer at a rate k_p. (B) Rogaratinib bind with an active dimer D_A at a rate $k^D_{C,on}$ to form D^C_A which dissociate at a rate $k^D_{C,off}$. These events lead to (1) inhibition of FGFR3 phosphorylation; and consequently, (2) inhibition of downstream signaling of AKT, MAPK, ERK and STAT.

References

[1] Siegel R, Miller K, Jemal A. 2020 Cancer statistics, 2020. CA Cancer J Clin **70**, 1, 7–30.

[2] Raghavan D. 2015 Chemotherapy for invasive bladder cancer: Five simple rules learned over 30 years. Bladder Cancer **1**, 1, 3–13.

[3] Chang J, Lara P, Pan CX. 2012 Progress in personalizing chemotherapy for bladder cancer. Adv in Urol **2012**. (doi:10.1155/2012/364919).

[4] Casadei C, Dizman N, Schepisi G, Cursano M, Basso U, Santini D, Pal S, Giorgi UD. 2019 Targeted therapies for advanced bladder cancer: new strategies with fgfr inhibitors. Ther Adv Med Oncol **11**. (doi:10.1177/1758835919890285).

[5] Sheepbouwer C, Meyer S, Burggraaf J, Jose J, Molfhoff C. 2016 A multimodal imaging approach for longitudinal evaluation of bladder tumor development in an orthotopic murine model. PLoS ONE **11**, 8, e0161284.

[6] Qin W, Hu L, Zhang X, Jiang S, Lj J, Zhang Z, Wang X. 2019 The diverse function of pd-1/pd-l pathway beyond cancer. Front Immunol **10**, 2298. (doi:10.3389/fimmu.2019.02298).

[7] Hsu F, Su C, Huang K. 2017 A comprehensive review of us fda-approved immune checkpoint inhibitors in urothelial carcinoma. J Immuno Res **2017**. (doi:https://doi.org/10.1155/2017/6940546).

[8] Kacew A, Sweis RF. 2020 Fgfr3 alterations in the era of immunotherapy for urothelial bladder cancer. Front Immunol **11**, 575258. (doi:doi:10.3389/fimmu.2020.575258).

[9] Jain HV, Jackson TL. 2018 Mathematical modeling of cellular cross-talk between endothelial and tumor cells highlights counterintuitive effects of vegf-targeted therapies. Bull Math Biol **80**, 5, 971–1016. (doi:10.1007/s11538-017-0273-6).

[10] Storey KM, Lawler SE, Jackson TL. 2020 Modeling oncolytic viral therapy, immune checkpoint inhibition, and the complex dynamics of innate and adaptive immunity in glioblastoma treatment. Front Physiol **11**, 151. (doi:10.3389/fphys.2020.00151).

[11] Kuznetsov V, Makalkin I, Taylor M, Perelson A. 1994 Nonlinear dynamics of immunogenic tumors: parameter estimation and global bifurcation analysis. Bull Math Biol **52**, 2, 295–321.

[12] Nikolopoulou E, Eikenberry SE, Gevertz JL, Kuang Y. 2017 Mathematical modeling of an immune checkpoint inhibitor and its synergy with an immunostimulant. DCSB-B **22**, 11. (doi:10.3934/dcdsb.2020138).

[13] Lai X, Friedman A. 2017 Combination therapy of cancer with cancer vaccine and immune checkpoint inhibitors: A mathematical model. PLoS ONE **12**, 5, e0178479.

[14] Zhao B, Zhang C, Forsten-Williams K, Zhang J, Fannon M. 2010 Endothelial cell capture of heparin-binding growth factors under flow. PLoS Comput Biol **6**, 10, e1000971.

[15] Olwin B, Hauschka S. 1988 Cell surface fibroblast growth factor and epidermal growth factor receptors are permanently lost during skeletal muscle terminal differentiation in culture. J Cell Biol **107**, 761–769.

[16] Nikolopoulou E, Johnson L, Harris D, Nagy J, Stites E, Kuang Y. 2018 Tumour-immune dynamics with an immune checkpoint inhibitor. Letters in Biomathematics **5**, supl1, S137–S159. (doi:DOI:10.1080/23737867.2018.1440978).

[17] Grünewald S, Politz O, Bender S, Héroult M, Lustig K, et al UT. 2019 Rogaratinib: A potent and selective pan-fgfr inhibitor with broad antitumor activity in fgfr-overexpressing preclinical cancer models. Int J Cancer **45**, 5, 1346–1357.

[18] Schuler M, Cho B, Sayehli C, Navarro A, Soo R, et al HR. 2019 Rogaratinib in patients with advanced cancers selected by fgfr mrna expression: a phase 1 dose-escalation and dose-expansion study. The Lancet Oncology **20**, 10, 1454–1466. (doi:10.1016/S1470-2045(19)30412-7).

[19] Collin MP, Lobell M, Hübsch W, Brohm D, Schirok H, Jautelat R, Lustig K, Bömer U, Vöhringer V, Héroult M, et al. 2018 Discovery of rogaratinib (bay 1163877): a pan-fgfr inhibitor. ChemMedChem **13**, 5, 437–445.

[20] Cariboni J, Gatelli D, Liska R, Saltelli A. 2007 The role of sensitivity analysis in ecological modelling. Ecological Modelling **203**, 1-2, 167–182.

[21] Blower SM, Dowlatabadi H. 1994 Sensitivity and uncertainty analysis of complex models of disease transmission: an hiv model, as an example. Int Stat Rev **62**, 2, 229–243,.

[22] Marino S, Hogue IB, Ray CJ, Kirschner DE. 2008 A methodology for performing global uncertainty and sensitivity analysis in systems biology. J Theoret Biol **254**, 1, 178–196.

[23] Eisenburg M, Jain H. 2017 A confidence building exercise in data and identifiability: Modeling cancer chemotherapy as a case study. J Theor Biol **431**, 63–78.

[24] Gabor A, Villaverde A, Banga J. 2017 Parameter identifiability analysis and visualization in large-scale kinetic models of biosystems. BMC Sys Biol **11**. (doi:10.1186/s12918-017-0428-y).

[25] Gallaher J, Larripa K, Renardy M, Shtylla B, Tania N, White D, Wood K, Zhu L, Passey C, Robbins M, et al. 2018 Methods for determining key components in a mathematical model

for tumor–immune dynamics in multiple myeloma. J Theoret Biol **458**, 31–46. (doi:https://doi.org/10.1016/j.jtbi.2018.08.037).

[26] Meshkat N, z Kuo CE C, III JD. 2014 On finding and using identifiable parameter combinations in nonlinear dynamic systems biology models and combos: A novel web implementation. PLoS ONE **9**, 10, e110261,.

[27] Chis OT, Banga J, Balsa-Canto E. 2011 Structural identifiability of systems biology models: a critical comparison of methods,. PLoS ONE **6**, 11, e27755.

[28] Raue A, Kreutz C, Maiwald T, Bachmann J, Schilling M, KlingmÃŒller U, Timmer J. 2009 Structural and practical identifiability analysis of partially observed dynamical models by exploiting the profile likelihood. Bioinformatics **25**, 25, 1923–1929.

[29] Goel M, Khanna P, Kishore J. 2010 Understanding survival analysis: Kaplan-meier estimate. Int J Ayurveda Res **1**, 4, 274–278.

[30] Dovedi S, Davies B. 2009 Emerging targeted therapies for bladder cancer: a disease waiting for a drug. Cancer Metastasis Rev **28**, 3-4, 355–367.

[31] Stenehjem D, Tran D, Nkrumah M, Gupta S. 2018 Pd1/pdl1 inhibitors for the treatment of advanced urothelial bladder cancer. Onco Targets Ther **11**, 5973–5989.

[32] Fassan M, Trabulsi E, Gomella L, Baffa R. 2007 Targeted therapies in the management of metastatic bladder cancer. Biologics **1**, 4, 333–406.